NONRECIPROCAL COUPLING TO MICROSTRIP RESONATORS

BY

CHRISTOPHER W PETERSON

THESIS

Submitted in partial fulfillment of the requirements
for the degree of Master of Science in Electrical and Computer Engineering
in the Graduate College of the
University of Illinois at Urbana-Champaign, 2018

Urbana, Illinois

Adviser:

Assistant Professor Gaurav Bahl

Abstract

Inducing nonreciprocal wave propagation is a fundamental challenge across a wide range of physical systems in electromagnetics, optics, and acoustics. Linear, time-invariant systems are always reciprocal, but reciprocity can be broken through the action of a bias that is asymmetric under time-reversal. Magnetic fields are the most common bias used to produce nonreciprocal devices. However, nonreciprocal devices using magnetic fields are difficult to integrate into larger systems that may be sensitive to magnetic fields. To overcome this challenge, recent efforts to create nonreciprocal devices have instead exploited momentum-based techniques such as coherent spatiotemporal modulation of resonators and waveguides. One such technique, indirect interband scattering, uses a traveling wave bias to scatter light between two modes which differ in frequency and momentum. Due to momentum conservation, this process is inherently nonreciprocal — light traveling in different directions will be scattered differently by the traveling wave bias. This thesis extends the method of indirect interband scattering in two separate domains. Indirect interband scattering has so far been demonstrated only between co-propagating traveling modes, both in waveguides and whispering-gallery-mode resonators. Here, indirect scattering between a waveguide and standing-mode resonator is described and demonstrated experimentally. There are several capabilities and advantages unique to this type of indirect scattering, which we term "nonreciprocal coupling". Additionally, while indirect scattering has so far mainly been explored in optical systems, the experiments in this thesis occur in the microwave frequency domain.

Acknowledgments

I acknowledge funding support from the US Office of Naval Research (grant N00014-16-1-2830), the National Science Foundation Emerging Frontiers in Research and Innovation NewLAW program (grant EFMA-1627184), and a National Science Foundation Graduate Research Fellowship.

I thank my advisor, Prof. Gaurav Bahl, for his guidance, and my colleagues for helpful discussions. Special thanks to Prof. Jennifer Bernhard for allowing me to use her lab's resources for my research.

Thanks also to my family, for setting me on this path and providing a stable foundation from which I could explore.

Finally, thanks to my girlfriend, Addie, who has shown patience and love in supporting my graduate studies.

Contents

Chapter 1

Introduction

This chapter provides the background necessary to understand the remainder of the thesis, which focuses on extending the idea of indirect interband photonic transitions to a new regime - between waveguides and resonators. First, the concepts of reciprocity and nonreciprocity are introduced, beginning from Maxwell's equations. A brief history of indirect interband photonic transitions and their use in creating nonreciprocal devices is presented. Finally, motivations for the research presented in this thesis are discussed. The basis for the research presented in this thesis was first published in Ref. [1].

1.1 Reciprocity

In general, reciprocity of wave propagation means that waves traveling in opposite directions behave identically [2]. In electromagnetics there are two formulations of reciprocity that both can be derived directly from Maxwell's equations.

Consider the electromagnetic field $[\boldsymbol{E}_1, \boldsymbol{H}_1]$ produced by the source $[\boldsymbol{J}_1, \boldsymbol{M}_1]$, and the field $[\boldsymbol{E}_2, \boldsymbol{H}_2]$ produced by the source $[\boldsymbol{J}_2, \boldsymbol{M}_2]$, where $\boldsymbol{E}$ is the electric field, $\boldsymbol{H}$ is the magnetic field, $\boldsymbol{J}$ is the electric current density, and $\boldsymbol{M}$ is the (fictitious) magnetic current density (bold symbols are both time-harmonic phasors and vectors). Maxwell's equations in differential form for these fields are

$$\begin{aligned} \nabla \times \boldsymbol{E}_1 &= -j\omega\mu \boldsymbol{H}_1 - \boldsymbol{M}_1 \ , \\ \nabla \times \boldsymbol{H}_1 &= j\omega\epsilon \boldsymbol{E}_1 + \sigma \boldsymbol{E}_1 + \boldsymbol{J}_1 \ , \end{aligned} \tag{1.1}$$

$$\begin{aligned} \nabla \times \boldsymbol{E}_2 &= -j\omega\mu \boldsymbol{H}_2 - \boldsymbol{M}_2 \ , \\ \nabla \times \boldsymbol{H}_2 &= j\omega\epsilon \boldsymbol{E}_2 + \sigma \boldsymbol{E}_2 + \boldsymbol{J}_2 \ , \end{aligned} \tag{1.2}$$

where ϵ is the permittivity, μ is the permeability, and σ is the conductivity of the medium. All medium parameters vary with position $\vec{r}$, and are assumed to be linear and time-invariant. These equations can be combined to form the *reciprocity theorem in integral form* [3] by applying Gauss' theorem to a surface S enclosing a finite volume V

$$\begin{aligned} &\oiint_S (\boldsymbol{H}_2 \times \boldsymbol{E}_1 - \boldsymbol{H}_1 \times \boldsymbol{E}_2) \cdot dS \\ &\qquad = \iiint_V (\boldsymbol{E}_1 \cdot \boldsymbol{J}_2 + \boldsymbol{H}_2 \cdot \boldsymbol{M}_1 - \boldsymbol{E}_2 \cdot \boldsymbol{J}_1 - \boldsymbol{H}_1 \cdot \boldsymbol{M}_2) dV \ . \end{aligned} \tag{1.3}$$

There are two special cases of this equation, respectively called *Lorentz reciprocity* and *Rayleigh-Carson reciprocity* [3, 4]. In a region with all the sources (if the volume is taken to infinity) or no sources, both sides of Eq. (1.3) are equal to zero and the equation can be rewritten

$$\oiint_S (\boldsymbol{H}_2 \times \boldsymbol{E}_1) \cdot dS = \oiint_S (\boldsymbol{H}_1 \times \boldsymbol{E}_2) \cdot dS \ . \tag{1.4}$$

This form, known as the *Lorentz reciprocity theorem*, gives an equivalence between the electric and magnetic fields on a surface enclosing the region. Under the same assumption, Eq. (1.3) can also be rewritten as

$$\iiint_V (\boldsymbol{E}_1 \cdot \boldsymbol{J}_2 - \boldsymbol{H}_1 \cdot \boldsymbol{M}_2) dV = \iiint_V (\boldsymbol{E}_2 \cdot \boldsymbol{J}_1 - \boldsymbol{H}_2 \cdot \boldsymbol{M}_1) dV \ , \tag{1.5}$$

which is known as the *Rayleigh-Carson reciprocity theorem*. This equation can be simplified by removing the magnetic currents (which do not exist in reality)

$$\iiint_V \boldsymbol{E}_1 \cdot \boldsymbol{J}_2 dV = \iiint_V \boldsymbol{E}_2 \cdot \boldsymbol{J}_1 dV \ . \tag{1.6}$$

The above reciprocity theorems, derived directly from Maxwell's equations, show a

relation between the fields produced by different sources within the same volume. However, these formulations are not directly usable for many applications.

To produce a more directly applicable formulation of reciprocity, the Rayleigh-Carson reciprocity theorem can be further simplified when applied to networks defined by ports. We define a port n by a point-like current I_n and voltage V_n. Equation (1.6) can be rewritten for a network of such ports as

$$\sum_n V_n^1 I_n^2 = \sum_n V_n^2 I_n^1 \tag{1.7}$$

where V_n^m is the voltage on port n from applied current I_n^m. If we consider a two port network where $I^1 = I_1^0$ and $I^2 = I_2^0$ (an identical current applied to either port 1 or 2), this equation reads

$$V_2 = V_1 \ . \tag{1.8}$$

Equation (1.8) states that *the voltage at port 2 from a current at port 1 is identical to the voltage at port 1 from the same current at port 2.* This basic rule of reciprocity can be extended to networks with more than two ports, and is the more easily understood statement of reciprocity.

The currents and voltages at the ports of an N-port network can be compiled into column vectors (borrowing the bra-ket notation from quantum mechanics)

$$|i\rangle = \begin{pmatrix} I_1 \\ \vdots \\ I_N \end{pmatrix} \ , |v\rangle = \begin{pmatrix} V_1 \\ \vdots \\ V_N \end{pmatrix} \ , \tag{1.9}$$

which follow the relation

$$|v\rangle = \hat{Z}\,|i\rangle \ . \tag{1.10}$$

The matrix $\hat{Z}$ is known as the impedance matrix and it follows from Eq. (1.7) that, for reciprocal networks, $\hat{Z}$ must be symmetric ($\hat{Z} = \hat{Z}^T$). This can be shown by

rewriting Eq. (1.7) in bra-ket notation

$$\langle v_1^* | i_2 \rangle = \langle v_2^* | i_1 \rangle \ . \tag{1.11}$$

Using the definition of the impedance matrix $\langle v^* | = \langle i^* | \, \hat{Z}^T$, this equation takes the form

$$\langle i_1^* | \hat{Z}^T | i_2 \rangle = \langle i_2^* | \hat{Z}^T | i_1 \rangle \ . \tag{1.12}$$

Since both sides are simply a complex number, the left-hand side can be transposed without changing the relation such that

$$\langle i_2^* | \hat{Z} | i_1 \rangle = \langle i_2^* | \hat{Z}^T | i_1 \rangle \ . \tag{1.13}$$

which clearly shows that the matrix $\hat{Z}$ must be symmetric ($\hat{Z} = \hat{Z}^T$).

In addition to the impedance matrix definition of a network, it is often more useful to define a network by its scattering matrix $\hat{S}$, where

$$| v_- \rangle = \hat{S} \, | v_+ \rangle \ . \tag{1.14}$$

The kets $|v_-\rangle$ and $|v_+\rangle$ represent output and input voltages from the ports, respectively. These voltages can be interpreted as the amplitudes of incoming and outgoing voltage waves at each port. The diagonal terms of the scattering matrix describe the reflection from each port, while the off-diagonal terms describe transmission between ports. Defined in this manner, the scattering matrix is related to the impedance matrix [5] as

$$\hat{S} = (\hat{Z} + \hat{I})^{-1} (\hat{Z} - \hat{I}) \ , \tag{1.15}$$

where $\hat{I}$ is the identity matrix. Since $\hat{I} = \hat{I}^T$ and $\hat{Z} = \hat{Z}^T$, the scattering matrix for a reciprocal network obeys $\hat{S} = \hat{S}^T$. This definition of a reciprocal network — that its scattering matrix is symmetric — is widely used because a network is usually characterized by its scattering matrix. From this definition, reciprocity can be interpreted as the requirement that transmission between ports (e.g. from port $m \to n$, S_{nm}) is identical to transmission between the same ports in the opposite

direction (e.g. from port $n \to m$, $S_{mn} = S_{nm}$).

Although most networks are reciprocal there are many applications that require an asymmetric scattering matrix, or a system where reciprocity is broken. Such networks are known as *nonreciprocal* and can be created in a number of different ways. Recall that in the reciprocity theorems above we assumed that the medium was linear and time-invariant. Therefore time-varying systems are not required to be reciprocal, and we can imagine a nonreciprocal network that obeys

$$\hat{S}(t) = \hat{S}^T(-t) \ . \tag{1.16}$$

This is the relation that nonreciprocal systems based on the magneto-optic effect in gyrotropic materials [3, 6] obey. These systems can be understood by the relation [7]

$$\hat{S}(\boldsymbol{H}) = \hat{S}^T(-\boldsymbol{H}) \ , \tag{1.17}$$

where the magnetic field $\boldsymbol{H}$ is used as a bias which is asymmetric under time-reversal. However, using magnetic fields to break reciprocity creates inherent challenges if the created nonreciprocal devices must be integrated into larger systems, since magnetic fields often interfere with these larger systems and thus such nonreciprocal devices require bulky magnetic shielding. Due to these challenges, there has been recent interest in other methods of breaking reciprocity — including nonlinear [8, 9, 10, 11] as well as explicitly time-varying [12, 13, 14, 15, 16, 17, 18, 19, 20, 21, 22, 23, 24, 25, 26, 27, 28] techniques. The rest of this thesis will focus on a technique involving spatiotemporal modulation, where a bias is applied which varies in both space and time, that exploits a phenomenon known as indirect interband photonic transitions.

1.2 Indirect interband photonic transitions

Indirect interband photonic transitions are a phenomenon that can be exploited to produce nonreciprocity. This section presents a broad overview of the previous work on this topic: indirect electronic transitions, the analogy to indirect photonic

transitions, and how such transitions can be used to create nonreciprocal networks.

From the perspective of an electron, a crystal appears as a nearly infinite periodic array of atoms. Due to the approximately infinite nature of the crystal, the number of available states for electrons to occupy is also nearly infinite. The available states, mainly the outermost atomic orbitals, are spatially overlapping due to the short distance between atoms in the crystal. These overlapping states hybridize and their energy degeneracy lifts, forming energy bands with distributed wavefunctions [29]. These electronic energy bands can be described by the energy and momentum of the electrons occupying the band. For certain spacings of the atoms in the crystal lattice a gap can open where there are no available states in the energy bands: this is known as a bandgap [29].

There are broadly two types of band gaps: direct and indirect. In a direct bandgap the lowest energy state of the higher band has the same momentum as the highest energy state of the lower band, while in an indirect bandgap the states closest in energy differ in momentum (Fig. 1.1). Electrons can transition across a bandgap if they gain or lose energy by absorbing or emitting a photon, but because photons carry very little momentum in comparison to their energy this process primary occurs only if the bandgap is direct. For electrons to transition across an indirect bandgap there must be an additional exchange of momentum. Typically, this additional momentum comes from the creation or annihilation of a phonon, a vibration of the crystal lattice that has high momentum and low energy. This process is known as an indirect interband electronic transition.

The explicit analogy from indirect electronic transitions to indirect photonic transitions was first made in a 1999 paper by Winn et al. (Ref. [30]) in the context of photonic crystals, though similar ideas were proposed earlier [31, 32]. Photonic crystals are periodic arrays of alternating materials with strongly contrasting dielectric constants that mimic electronic crystals and can also have energy bands and bandgaps [33]. They proposed that photons (light) can be scattered between the energy bands of a photonic crystal if the refractive index is modulated in both time and space, provided that the modulation matches the frequency and momentum difference between the bands. This process may be achieved in nonlinear media through

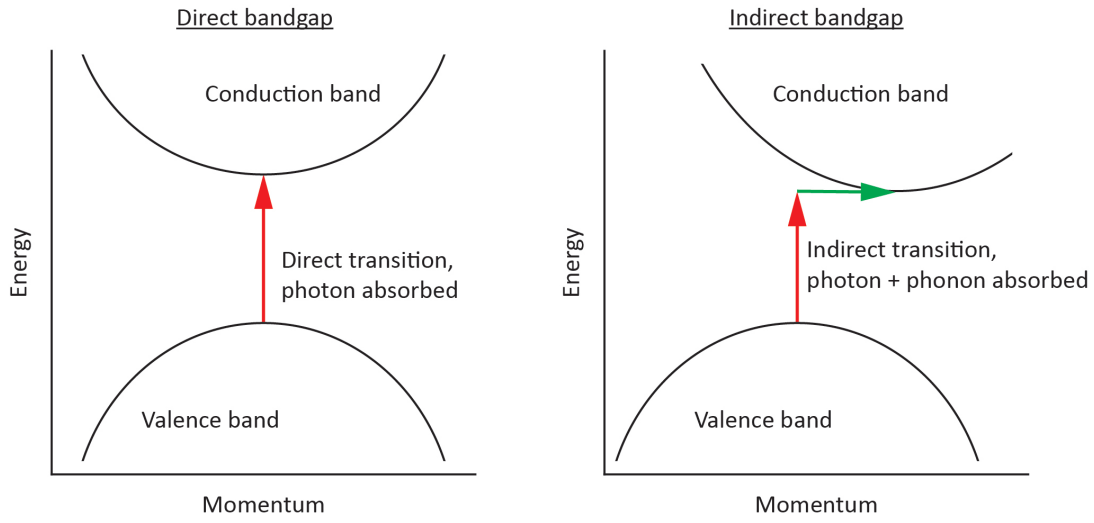

Figure 1.1: Electronic bandgaps can be either direct (left) or indirect (right). In a direct bandgap, transitions between the top of the valence band and bottom of the conduction band require no momentum shift and thus only require additional energy, usually absorbed from a photon (a particle with high energy and low momentum). In an indirect bandgap, transitions between the bands require a momentum shift, usually satisfied by absorption or emission of a phonon (a quasi-particle with low energy and high momentum) in addition to the photon.

a similar process as harmonic generation [34], where light perturbs the dielectric constant of a $\chi^{(2)}$ medium. However, this is not the only method for producing indirect interband photonic transitions — any process that modulates the refractive index in the appropriate manner will cause such transitions. For example, an experimental demonstration of indirect interband transitions in a silicon optical ring resonator [35] used a pulsed pump laser to generate free electron-hole pairs, which modified the refractive index in the appropriate manner.

A spatiotemporal modulation which generates indirect transitions and thus carries momentum necessarily breaks time-reversal symmetry, since momentum itself is asymmetric under time-reversal. Since indirect interband photonic transitions rely on this type of modulation, they can be used to create nonreciprocal devices. The idea to create nonreciprocity through indirect transitions was first proposed by Zongfu Yu and Shanhui Fan in a 2009 paper (Ref. [13]). The motivation behind this work is the inherent difficulty in on-chip integration of magneto-optic nonreciprocal devices [36]. In contrast, a nonreciprocal device based on indirect interband transitions could be produced in a CMOS-compatible process, and would not be restricted to specific power ranges as is the case with nonlinear nonreciprocal devices [13].

Amplitude nonreciprocity can be quantified through a parameter known as *isolation contrast*. The power isolation contrast I_{mn} between ports m and n is

$$I_{mn} = \frac{|S_{mn}|^2}{|S_{nm}|^2} \ , \tag{1.18}$$

or in dB form

$$I_{mn}^{[\mathrm{dB}]} = 20\log_{10}|S_{mn}| - 20\log_{10}|S_{nm}| \ . \tag{1.19}$$

Complete isolation refers to the case where the isolation contrast is $\pm\infty$ dB, meaning that there is zero transmitted power in one direction and finite transmitted power in the other. It can be shown mathematically that indirect interband photonic transitions can lead to complete optical isolation. Following Ref. [13], consider a two-dimensional optical waveguide that is uniform and infinite in the z direction. Such a waveguide hosts both symmetric and anti-symmetric modes that can be classified

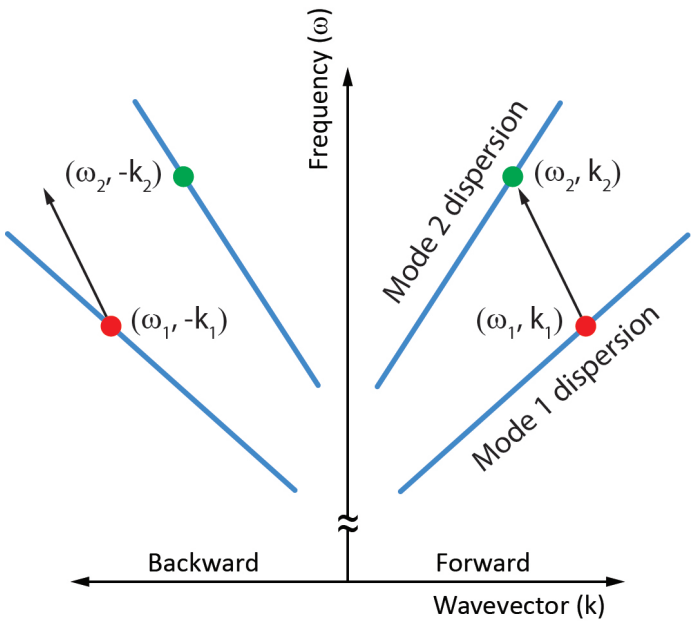

Figure 1.2: Illustration of the dispersion of two modes in an electromagnetic waveguide. These "photonic" modes can be coupled by a spatiotemporal modulation which matches their frequency and momentum (wavevector) difference, similarly to how indirect electronic transitions can occur. These transitions are inherently nonreciprocal because the momentum matching only works for one direction of propagation (here, the forward direction).

by their frequencies and wavevectors (ω_1, k_1) and (ω_2, k_2), as pictured in Fig. 1.2. A spatiotemporal modulation of the dielectric constant of the medium that the waves propagate in is given by

$$\epsilon'(x, z, t) = \alpha(x) \cos(\Omega t - (-q)z) \ , \tag{1.20}$$

where $\alpha(x)$ is the spatially dependent amplitude of the modulation. As previously discussed, for the modulation to produce indirect interband transitions (scatter light between the two modes of the waveguides), the frequency of modulation must equal the frequency difference between the modes, $\Omega = \omega_2 - \omega_1$. Additionally, the wavevector of the modulation (proportional to momentum) must equal the wavevector difference between the modes, $q = k_2 - k_1$. To account for modulation with a slightly different wavevector it is useful to introduce the variable $\Delta k = k_2 - k_1 + q$. The electric field in the waveguide can be written

$$E(x, z, t) = a_1(z)E_1(x)e^{i(-k_1 z + \omega_1 t)} + a_2(z)E_2(x)e^{i(-k_2 z + \omega_2 t)} \ , \tag{1.21}$$

where $a_{1,2}$ are the amplitudes and $E_{1,2}$ are the spatial profiles of the two waveguide modes. Using the slowly varying amplitude approximation [37], Maxwell's equations can be solved for these electric fields through the coupled-mode equation [38]

$$\frac{d}{dz}\begin{pmatrix} a_1 \\ a_2 \end{pmatrix} = \begin{pmatrix} 0 & jCe^{-j\Delta k z} \\ jCe^{j\Delta k z} & 0 \end{pmatrix}\begin{pmatrix} a_1 \\ a_2 \end{pmatrix} \ , \tag{1.22}$$

where

$$C = \frac{\epsilon_0}{8}\int_{-\infty}^{\infty} \alpha(x)E_1(x)E_2(x)dx \ , \tag{1.23}$$

which is an overlap integral between the two modes and the applied modulation. Given the initial condition that only mode 1 is excited, $a_1(0) = 1,\ a_2(0) = 0$, the

solution to Eq. (1.22) is

$$\begin{aligned} a_1(z) &= e^{-jz\Delta k/2}\Big[\cos\left(z\sqrt{C^2+(\Delta k/2)^2}\right) \\ &\qquad + j\frac{\Delta k}{2\sqrt{C^2+(\Delta k/2)^2}}\sin\left(z\sqrt{C^2+(\Delta k/2)^2}\right)\Big] \ , \\ a_2(z) &= je^{jz\Delta k/2}\frac{C\sin\left(z\sqrt{C^2+(\Delta k/2)^2}\right)}{\sqrt{C^2+(\Delta k/2)^2}} \ . \end{aligned} \tag{1.24}$$

In the case of perfect phase matching, $\Delta k = 0$, this reduces to

$$\begin{aligned} a_1(z) &= \cos(zC) \ , \\ a_2(z) &= j\sin(zC) \ , \end{aligned} \tag{1.25}$$

and an incident wave in mode 1 will completely transition to mode 2 over a length $\ell_c = \pi/(2C)$. In the opposite direction the phase matching condition is not satisfied, since $(-k_2) - (-k_1) + q \neq \Delta k$. Therefore the indirect transition only occurs for one direction, creating a nonreciprocal device. This device follows the nonreciprocal scattering matrix definition described in the previous section,

$$\boldsymbol{S}(q) = \boldsymbol{S}^T(-q) \ , \tag{1.26}$$

since $(-k_2) - (-k_1) + (-q) = -(k_2 - k_1 + q) = -\Delta k$.

Indirect interband scattering has been extended beyond the original proposal of a two-dimensional waveguide to create a variety of nonreciprocal devices. The phenomenon has been observed experimentally in both waveguides [17, 15, 18] and resonators [22, 23, 26, 39]. Coupling has been shown between optical modes [17, 15, 18, 39], between an optical and an acoustic mode [22, 23, 26], and can be realized between two acoustic modes [40]. Despite the variety of methods and types of waves with which nonreciprocity through indirect interband transitions has been realized, limitations remain. This thesis aims to remove some of these limitations as well as introduce new nonreciprocal capabilities based on indirect interband transitions.

1.3 Motivation and scope of this work

As discussed in the previous section, indirect interband transitions are a powerful tool for creating nonreciprocal devices without the challenges associated with gyrotropic or non-linear media. However, nonreciprocal devices based on indirect photonic transitions have so far been limited because such devices exclusively rely on scattering between co-propagating modes in wave-guides [13, 17, 15, 18, 40] or resonators [22, 23, 26, 39]. Mainly, the use of co-propagating modes has resulted in all the demonstrated devices having nonreciprocal transfer functions that are restricted to a Lorentzian-shaped frequency response. Co-propagating modes exist in the same medium, limiting the degrees of freedom (DOFs) that could be tuned to produce customizable higher-order frequency responses, which require multiple DOFs [5, 41, 42, 43]. Using co-propagating resonant modes adds an additional parameter, the quality factor of the modes used, but with only two modes it remains impossible to produce higher-order nonreciprocal transfer functions.

This thesis proposes that indirect transitions can also be induced between a guided mode and a stationary resonant mode. The indirect transitions are produced through spatiotemporal modulation of spatially distributed coupling sites between the guided and resonant mode. Such modulation is termed "synthetic phonons" since it emulates the action of phonons with high momentum and low frequency and is realized through phased modulation of coupling sites, analogous to the modulation of lattice sites that constitutes phonons in a crystal. The indirect transitions effectively generate *nonreciprocal coupling* between the guided and resonant mode, as light propagating in different directions is coupled to the resonance differently. It will be shown nonreciprocal coupling enables nonreciprocal devices with highly tailorable, reconfigurable transfer functions that can be arranged using conventional waveguides and resonators.

It is important to note a major difference between indirect transitions among co-propagating modes and nonreciprocal coupling between a guided and resonant mode. In a closed system, co-propagating modes in a waveguide or resonator are orthogonal and thus, by definition, are not coupled unless by an applied bias. In contrast,

resonant modes often couple to guided modes. This coupling is reciprocal, making it undesirable in systems utilizing nonreciprocal coupling. To ensure that nonreciprocal coupling is not disturbed by this "reciprocal coupling", it is useful to intentionally create a phase mismatch between the guided and resonant modes. Throughout this thesis such phase mismatched resonant modes are referred to as dark states because, analogous to atomic dark states [44, 45], they are localized resonances that cannot emit or absorb light. These dark states are an example of parametric bound states in the continuum (BICs) [46, 47], where the tuning parameter to produce the BIC is the separation between coupling sites. Dark states have previously been studied for applications in photonics [48, 49, 50] and have several properties, namely suppressed emission and long lifetime, that are especially useful for creating nonreciprocal devices.

Chapter 2 of this thesis focuses on the theory of nonreciprocal coupling. It will review temporal coupled-mode theory as applied to waveguide-resonator systems, describe how phase mismatched resonant modes (dark states) can be produced, and propose a method for producing indirect transitions between waveguides and these dark states. Chapter 3 presents experimental evidence of nonreciprocal coupling in microstrip circuits. First, this chapter reviews resonators and waveguides in microstrip circuits and technical details important to understanding time-varying coupling rates between such waveguides and resonators. It next provides experimental data which demonstrates nonreciprocal coupling to microstrip resonators, and experimental validation of the theory of operation. Chapter 4 proposes applications of nonreciprocal coupling and demonstrates experimentally how this nonreciprocal coupling can be used to produce fundamental nonreciprocal devices as well as higher-order nonreciprocal filters. Finally, Chapter 5 summarizes the work in this thesis and proposes future work that extends the concepts introduced.

Chapter 2

Nonreciprocal coupling: Theory

This chapter presents a theoretical analysis of nonreciprocal coupling using the framework of temporal coupled-mode theory. It reviews temporal coupled-mode theory as applied to waveguide-resonator systems, describes how phase mismatched resonant modes (dark states) can be produced, and proposes a method for producing indirect transitions between waveguides and these dark states.

2.1 Temporal coupled mode theory

Coupled-mode theory is an important and widely used technique for calculating how energy is transferred between coupled modes, which can be either guided or resonant modes. This section will present an overview of temporal coupled mode theory, which will be used later in this chapter to show how resonant states can be engineered into dark states and how coupling can be engaged to such dark states nonreciprocally. A review of the history of coupled-mode theory can be found in Ref. [51]. For the purposes of this thesis, the temporal coupled-mode theory presented in Refs. [38, 52, 53], which make use of the slowly varying amplitude approximation [37], is adequate. In the following, the Dirac's bra-ket notation is used to denote a vector (e.g. a vector $|x\rangle$), and matrices are denoted by a "hat" (e.g. a matrix $\hat{A}$).

Consider a system with n resonant modes. Following Ref. [53], the time-varying amplitude of each mode can be modeled by the differential equation

$$\frac{d\,|a\rangle}{dt} = j\hat{\Omega}\,|a\rangle \ . \tag{2.1}$$

Here $|a\rangle$ is a vector of length n which representing the mode amplitudes of the resonant modes

$$|a\rangle = \begin{pmatrix} a_1 \\ a_2 \\ \vdots \\ a_n \end{pmatrix} , \tag{2.2}$$

and $\hat{\Omega}$ is an $n \times n$ matrix which describes the resonant frequencies and coupling between the modes

$$\hat{\Omega} = \begin{pmatrix} \omega_{0,1} & \omega_{12} & \dots & \omega_{1n} \\ \omega_{21} & \omega_{0,2} & \dots & \omega_{2n} \\ \vdots & & \ddots & \\ \omega_{n1} & \omega_{n2} & \dots & \omega_{0,n} \end{pmatrix} . \tag{2.3}$$

If the coupling between the resonant modes is reciprocal, this matrix is symmetric. Each diagonal term $\omega_{0,n}$ is the resonant frequency of the n^{th} mode, and the off-diagonal terms ω_{n_1,n_2} describe direct coupling between modes n_1 and n_2. As will be shown later, it is also possible to create indirect coupling between the modes through interactions with a waveguide. Although Ref. [53] only considers lossless resonant modes, such modes are impossible to realize in practice. To account for the intrinsic losses in the resonant modes, we can introduce a diagonal matrix $\hat{\kappa}$,

$$\hat{\kappa} = \begin{pmatrix} \kappa_1 & 0 & \dots & 0 \\ 0 & \kappa_2 & \dots & 0 \\ \vdots & & \ddots & \\ 0 & 0 & \dots & \kappa_n \end{pmatrix} , \tag{2.4}$$

such that

$$\frac{d\,|a\rangle}{dt} = \left(j\hat{\Omega} - \hat{\kappa}\right)|a\rangle \ . \tag{2.5}$$

If the n resonant modes are coupled to m ports (e.g. ports of the network discussed

in Chapter 1), the resulting system can be modeled through the equations

$$\frac{d\left|a\right\rangle}{dt} = \left(j\hat{\Omega} - \hat{\kappa} - \hat{\Gamma}\right)\left|a\right\rangle + \hat{K}^T\left|s_+\right\rangle \tag{2.6}$$

and

$$\left|s_-\right\rangle = \hat{C}\left|s_+\right\rangle + \hat{D}\left|a\right\rangle \ . \tag{2.7}$$

The vectors $|s_+\rangle$ and $|s_-\rangle$ respectively describe the input and output fields at the ports (numbered $1 \to m$) and are related to each other through the *scattering matrix* $\hat{S}$ as

$$\left|s_-\right\rangle = \hat{S}\left|s_+\right\rangle \ , \tag{2.8}$$

where

$$\left|s_+\right\rangle = \begin{pmatrix} s_{1+} \\ s_{2+} \\ \vdots \\ s_{m+} \end{pmatrix} \ , \tag{2.9}$$

$$\left|s_-\right\rangle = \begin{pmatrix} s_{1-} \\ s_{2-} \\ \vdots \\ s_{m-} \end{pmatrix} \ , \tag{2.10}$$

and

$$\hat{S} = \begin{pmatrix} S_{11} & S_{12} & \dots & S_{1m} \\ S_{21} & S_{22} & \dots & S_{2m} \\ \vdots & & \ddots & \\ S_{m1} & S_{m2} & \dots & S_{mm} \end{pmatrix} \ . \tag{2.11}$$

The relation between any input s_{a+} and any output s_{b-} is

$$s_{b-} = S_{ba}s_{a+} \ . \tag{2.12}$$

Defined in this manner, a network of ports and resonant modes is nonreciprocal if

$\hat{S} \neq \hat{S}^T$. The matrix elements of the scattering matrix can be obtained by solving for the ratio s_{b-}/s_{a+}.

Returning to Equations (2.6) and (2.7), there are several additional matrices that must be defined, $\hat{\Gamma}$, $\hat{K}$, $\hat{C}$, and $\hat{D}$. Along with $\hat{\Omega}$, these matrices define the system their combination creates the scattering matrix $\hat{S}$. The $\hat{\Gamma}$ matrix,

$$\hat{\Gamma} = \begin{pmatrix} \gamma_1 & \gamma_{12} & \cdots & \gamma_{1n} \\ \gamma_{21} & \gamma_2 & \cdots & \gamma_{2n} \\ \vdots & & \ddots & \\ \gamma_{n1} & \gamma_{n2} & \cdots & \gamma_n \end{pmatrix}, \tag{2.13}$$

defines the decay of the resonant modes to the ports (the diagonal terms $\gamma_1 \rightarrow \gamma_n$), as well as coupling between the modes (the off-diagonal terms) that is caused by interactions with the ports. As can be seen in Equations (2.6) and (2.7), the interactions with the ports are captured by the $\hat{K}$ and $\hat{D}$ matrices. In Ref. [53] it is shown that $\hat{K} = \hat{D}$ due to time-reversal symmetry and although the systems we will analyze are nonreciprocal, time-reversal symmetry is preserved in the form $\hat{S}(t) = \hat{S}^T(-t)$ and the requirement that $\hat{K} = \hat{D}$ remains. Therefore, only $\hat{K}$ is used in the following. The matrix $\hat{K}$ is an $m \times n$ matrix

$$\hat{K} = \begin{pmatrix} k_{11} & k_{12} & \ldots & k_{1n} \\ k_{21} & k_{22} & \ldots & k_{2n} \\ \vdots & & \ddots & \\ k_{m1} & k_{m2} & \ldots & k_{mn} \end{pmatrix}, \tag{2.14}$$

where each term k_{ab} describes coupling between the a^{th} port and the b^{th} mode. Note that if the number of ports is not equal to the number of modes, $\hat{K}$ is not a square matrix. It is shown in Ref. [53] that, due to energy conservation, the coupling between the ports and modes is related to the decay rate of the modes through the relation $\hat{K}^\dagger \hat{K} = 2\hat{\Gamma}$. This relation can be used to calculate the coupling between resonant modes induced by interactions with the ports.

Finally, the matrix $\hat{C}$ is a scattering matrix that describes direct connections

between the ports. In a lossless and reciprocal system $\hat{C}$ must be respectively unitary and symmetric [53]. In this thesis, the direct connections between ports described by $\hat{C}$ will be referred to as "waveguides". In the following sections, the formalism presented in this section will be used to show how "dark states", resonances which are not coupled to any ports, can be created using destructive interference. It will then be shown how this coupling can be re-enabled nonreciprocally using spatiotemporal modulation referred to as "synthetic phonons".

2.2 Engineering dark states through destructive interference

Consider a representative system (Fig. 2.1a): two ports directly connected by a waveguide with a frequency-dependent propagation constant $\beta(\omega)$, and a resonator supporting a single mode at angular frequency ω_0. The resonator is side-coupled to the waveguide at N independent sites that are periodically separated on the waveguide by a constant length ℓ. For simplicity, assume that each coupling site is located at the same spatial location on the resonator, and that the waveguide is lossless and only supports a single mode. Forward propagation in the waveguide is defined as from port 1 toward port 2.

This system can be characterized by analyzing the coupling between the waveguide and the resonator using the framework of temporal coupled-mode theory as described in the previous section. Since each coupling site is independent, the coupling constants k_1 and k_2 (Fig. 2.1b) between the ports and resonator are evaluated as a superposition of the contributions from each site,

$$\begin{aligned} k_1 &= \sum_{n=1}^{N} c_n e^{-j\beta\ell(n-1)} \ , \\ k_2 &= \sum_{n=1}^{N} c_n e^{j\beta\ell(n-1)} \ , \end{aligned} \tag{2.15}$$

where c_n is the coupling constant at the n^{th} site. The exponential term in these

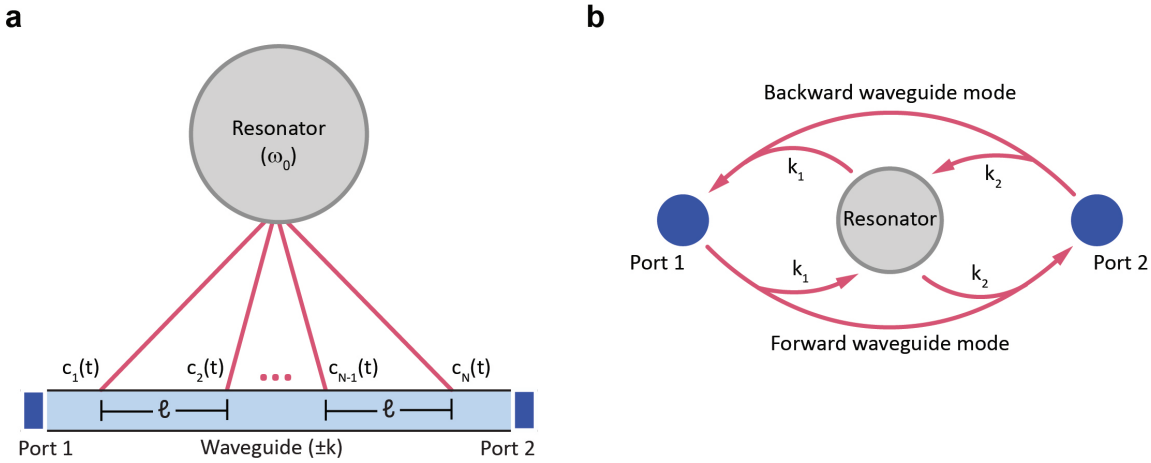

Figure 2.1: A resonator and two-port waveguide are coupled at multiple spatially separated sites.

definitions accounts for propagation in the waveguide between adjacent coupling sites spaced by ℓ, and differs between k_1 and k_2 due to the opposite propagation directions. As illustrated in Fig. 2.1b, k_1 describes coupling from the forward waveguide mode *into* the resonator and coupling *out of* the resonator to the backward waveguide mode. k_2 describes coupling from the backward waveguide mode *into* the resonator and coupling *out of* the resonator to the forward waveguide mode. As described in the previous section, the coupling constants are related to the resonator's decay, described by the decay rate to the ports

$$\gamma = \frac{|k_1|^2 + |k_2|^2}{2} \ . \tag{2.16}$$

Equation (2.15) reveals that the contribution to the total coupling constant from the n^{th} coupling site carries a phase $\beta\ell(n-1)$. When summed, these contributions interfere such that the maximum coupling rate occurs only if all N contributions are in-phase (phase matched coupling). Away from this maximum, the coupling rate decreases, reaching zero when the contributions perfectly destructively interfere. In the case of a complete phase mismatch, we obtain $\gamma = 0$ and the resonator can be classified as a dark state, or a bound state in the contiuum, since it cannot be excited

by or decay to the waveguide. Since phase matching in this system is determined by the product $\beta\ell$, it is possible to arrange a dark state from an arbitrary waveguide and resonator by selecting the appropriate ℓ.

2.3 Synthetic phonons enable nonreciprocal coupling

A dark state created by a total phase mismatch can be coupled to the accompanying waveguide through a synthetic phonon bias (Fig. 2.2). Recall from Chapter 1 that a synthetic phonon is a spatiotemporal variation of the coupling constants, in much the same way the phonons are spatiotemporal variations of atomic position. Consider synthetic phonons having angular frequency Ω, momentum q, and amplitude δ_c, which are written as a modulation of each site's coupling rate (illustrated in Fig. 2.2a)

$$c_n = c_0 + \delta_c \cos(\Omega t - q\ell(n-1)) \ . \tag{2.17}$$

The product $q\ell$ is simply a phase offset on the modulation applied to adjacent sites, thus any phonon momentum q can be selected by modulating each site with a phase offset $\theta_n = q\ell(n-1)$. The synthetic phonon bias breaks time-reversal symmetry, and thus induces nonreciprocal coupling, if the momentum q satisfies $q\ell \neq z\pi$, where z is an integer. This condition is equivalent to requiring synthetic phonons with a non-zero momentum, since if $q\ell = z\pi$ a standing wave is formed.

When this spatiotemporally modulated coupling is substituted into Eqs. (2.15) it is illustrative to separate the resulting terms into frequency components as follows:

$$\begin{aligned} k_1 = & \overbrace{c_0 \sum_{n=1}^{N} e^{-j\beta\ell(n-1)}}^{k_1^0} + \overbrace{\frac{c_M}{2} e^{j\Omega t} \sum_{n=1}^{N} e^{-j(\beta+q)\ell(n-1)}}^{k_1^+} \\ & + \overbrace{\frac{c_M}{2} e^{j\Omega t} \sum_{n=1}^{N} e^{-j(\beta-q)\ell(n-1)}}^{k_1^-} \ , \end{aligned} \tag{2.18}$$

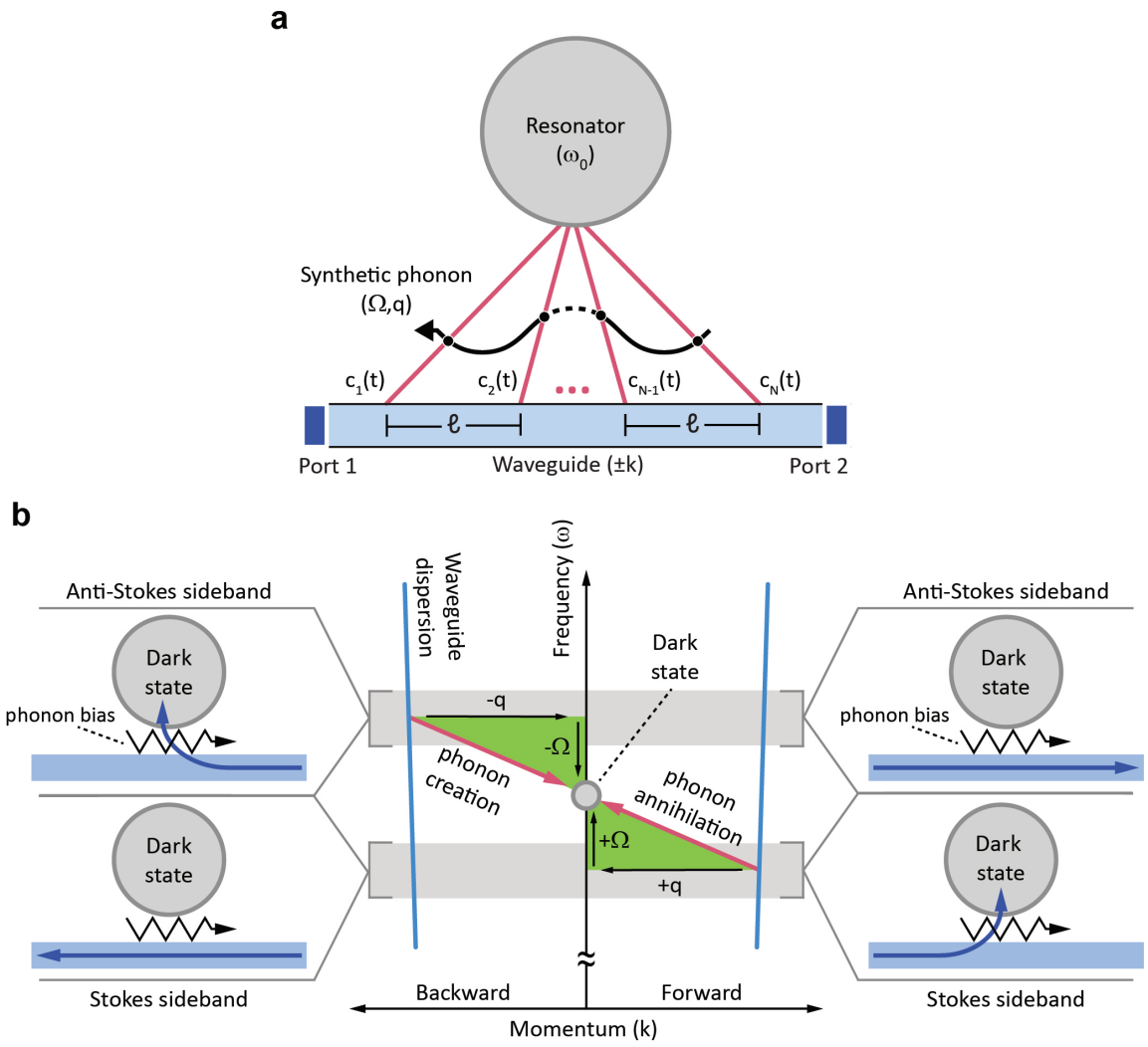

Figure 2.2: Theoretical description of nonreciprocal coupling. (a) A resonator and two-port waveguide are coupled at multiple spatially separated sites. The coupling at these sites is modulated to create synthetic phonons, which enable nonreciprocal coupling between the waveguide and resonator. (b) Interactions between photons and phonons enable coupling to photonic dark states by modifying the phase matching condition. Phonon-enabled coupling occurs only when the frequency and momentum difference between the waveguide mode and resonator mode are matched by the phonon frequency and momentum. This coupling is inherently nonreciprocal: the forward (right-traveling) guided mode only couples to the dark resonant state through phonon annihilation at the Stokes sideband frequency $(\omega_0 - \Omega)$, and the backward (left-traveling) guided mode only couples to the resonator through phonon creation at the anti-Stokes sideband frequency $(\omega_0 + \Omega)$.

$$k_2 = \overbrace{c_0 \sum_{n=1}^{N} e^{j\beta\ell(n-1)}}^{k_2^0} + \overbrace{\frac{c_M}{2} e^{j\Omega t} \sum_{n=1}^{N} e^{j(\beta-q)\ell(n-1)}}^{k_2^+} + \overbrace{\frac{c_M}{2} e^{-j\Omega t} \sum_{n=1}^{N} e^{j(\beta+q)\ell(n-1)}}^{k_2^-} . \tag{2.19}$$

For brevity, from here the terms that make up the coupling constants are referred to as $k_m = k_m^0 + k_m^+ + k_m^-$ for $m = 1, 2$. The first term, k_m^0, does not depend on the modulation amplitude δ_c and describes coupling which would occur without synthetic phonons. This coupling is zero in the case of a dark state. The remaining terms describe coupling enabled by interactions with synthetic phonons: k_m^+ corresponds to coupling where a synthetic phonon is annihilated and the photon shifts up in frequency, and k_m^- corresponds to coupling where a synthetic phonon is created and the photon shifts down in frequency. Due to energy and momentum conservation, both terms incorporate a frequency shift ($e^{\pm j\Omega t}$) and momentum shift ($\beta \pm q$), as depicted in Fig. 2.2b. The momentum shift modifies the original phase matching condition and can enable coupling to a resonator which would otherwise be dark. Additionally, note that the frequency shifted coupling constants are unequal ($k_1^\pm \neq k_2^\pm$) due to the directional momentum shift.

Coupling to the resonator, including coupling enabled by the action of synthetic phonons, has a significant impact on wave transmission through the waveguide due to resonant absorption or reflection. As described in the previous section, the scattering matrix (which describes the transmission and reflection coefficients) can be found using temporal coupled-mode theory as a function of the input frequency ω. As discussed in the previous section, the differential coupled-mode equation describing the resonant field a of a standing-wave resonator in the time-domain with inputs s_{1+} and s_{2+} is

$$\frac{da}{dt} = (j\omega_0 - \gamma - \kappa)a + jk_1 s_{1+} + jk_2 s_{2+} . \tag{2.20}$$

The output fields s_{2-}, s_{1-} are

$$\begin{aligned} s_{2-} &= e^{-j\beta\ell(N-1)}s_{1+} + jk_2 a \ , \\ s_{1-} &= e^{-j\beta\ell(N-1)}s_{2+} + jk_1 a \ . \end{aligned} \tag{2.21}$$

In these equations ω_0 is the resonance frequency, γ is the decay rate of the mode to the ports, κ is the intrinsic decay rate of the mode, and k_m is the effective coupling between port m and the resonant mode. The waveguide is matched to the ports and is lossless with a propagation constant β.

To find the scattering matrix elements S_{11} and S_{21} as function of the input frequency ω, we insert Eqs. (2.18) and (2.19) into Eq. (2.20), only considering inputs from port 1

$$\frac{da}{dt} = (j\omega_0 - \zeta)a + jk_1^0 s_{1+} + jk_1^+ s_{1+} + jk_1^- s_{1+} \ , \tag{2.22}$$

using $\zeta = \gamma + \kappa$. Since s_{1+} is time-harmonic with frequency ω and the coupling constants $k_1^{\pm}$ also have frequency components, we can rewrite this equation as

$$\frac{da}{dt} = (j\omega_0 - \zeta)a + jk_1^0 \tilde{s}_{1+} e^{j\omega t} + j\tilde{k}_1^+ \tilde{s}_{1+} e^{j(\omega+\Omega)t} + j\tilde{k}_1^- \tilde{s}_{1+} e^{j(\omega-\Omega)t} \ , \tag{2.23}$$

where $\tilde{x}$ signifies the time-invariant part of x. This is effectively a transformation from a system with modulated coupling to a system with three inputs at different frequencies. The steady-state solution to Eq. (2.23) is

$$\begin{aligned} a = &\frac{jk_1^0 \tilde{s}_{1+} e^{j\omega t}}{j(\omega - \omega_0) + \zeta} + \frac{j\tilde{k}_1^+ \tilde{s}_{1+} e^{j(\omega+\Omega)t}}{j(\omega + \Omega - \omega_0) + \zeta} \\ &+ \frac{j\tilde{k}_1^- \tilde{s}_{1+} e^{j(\omega-\Omega)t}}{j(\omega - \Omega - \omega_0) + \zeta} \ . \end{aligned} \tag{2.24}$$

Equation (2.24) shows that there are three components of the resonant field amplitude a, one at the original frequency ω and two sidebands at $\omega \pm \Omega$. These sidebands occur because the time-varying coupling rate amplitude-modulates the incoming signal.

The steady-state outputs at the ports can be found using Equations (2.24) and

(2.21) as

$$
\begin{aligned}
s_{2-} = s_{1+}\Bigg(& e^{-j\beta\ell(N-1)} - \frac{k_2^0 k_1^0}{j(\omega-\omega_0)+\zeta} - \frac{k_2^+ k_1^0}{j(\omega-\omega_0)+\zeta} \\
& - \frac{k_2^- k_1^0}{j(\omega-\omega_0)+\zeta} - \frac{k_2^0 k_1^+}{j(\omega+\Omega-\omega_0)+\zeta} \\
& - \frac{k_2^+ k_1^+}{j(\omega+\Omega-\omega_0)+\zeta} - \frac{k_2^- k_1^+}{j(\omega+\Omega-\omega_0)+\zeta} \\
& - \frac{k_2^0 k_1^-}{j(\omega-\Omega-\omega_0)+\zeta} - \frac{k_2^+ k_1^-}{j(\omega-\Omega-\omega_0)+\zeta} \\
& - \frac{k_2^- k_1^-}{j(\omega-\Omega-\omega_0)+\zeta}\Bigg),
\end{aligned}
\tag{2.25}
$$

and

$$
\begin{aligned}
s_{1-} = s_{1+}\Bigg(& e^{-j\beta\ell(N-1)} - \frac{k_1^0 k_1^0}{j(\omega-\omega_0)+\zeta} - \frac{k_1^+ k_1^0}{j(\omega-\omega_0)+\zeta} \\
& - \frac{k_1^- k_1^0}{j(\omega-\omega_0)+\zeta} - \frac{k_1^0 k_1^+}{j(\omega+\Omega-\omega_0)+\zeta} \\
& - \frac{k_1^+ k_1^+}{j(\omega+\Omega-\omega_0)+\zeta} - \frac{k_1^- k_1^+}{j(\omega+\Omega-\omega_0)+\zeta} \\
& - \frac{k_1^0 k_1^-}{j(\omega-\Omega-\omega_0)+\zeta} - \frac{k_1^+ k_1^-}{j(\omega-\Omega-\omega_0)+\zeta} \\
& - \frac{k_1^- k_1^-}{j(\omega-\Omega-\omega_0)+\zeta}\Bigg).
\end{aligned}
\tag{2.26}
$$

Using the definition of the scattering matrix elements, $S_{ab} = s_{a-}/s_{b+}$:

$$\begin{aligned} S_{21} = e^{-j\beta\ell(N-1)} &- \frac{k_2^0 k_1^0}{j(\omega-\omega_0)+\zeta} - \frac{k_2^+ k_1^0}{j(\omega-\omega_0)+\zeta} \\ &- \frac{k_2^- k_1^0}{j(\omega-\omega_0)+\zeta} - \frac{k_2^0 k_1^+}{j(\omega+\Omega-\omega_0)+\zeta} \\ &- \frac{k_2^+ k_1^+}{j(\omega+\Omega-\omega_0)+\zeta} - \frac{k_2^- k_1^+}{j(\omega+\Omega-\omega_0)+\zeta} \\ &- \frac{k_2^0 k_1^-}{j(\omega-\Omega-\omega_0)+\zeta} - \frac{k_2^+ k_1^-}{j(\omega-\Omega-\omega_0)+\zeta} \\ &- \frac{k_2^- k_1^-}{j(\omega-\Omega-\omega_0)+\zeta} \ , \end{aligned} \tag{2.27}$$

and

$$\begin{aligned} S_{11} = e^{-j\beta\ell(N-1)} &- \frac{k_1^0 k_1^0}{j(\omega-\omega_0)+\zeta} - \frac{k_1^+ k_1^0}{j(\omega-\omega_0)+\zeta} \\ &- \frac{k_1^- k_1^0}{j(\omega-\omega_0)+\zeta} - \frac{k_1^0 k_1^+}{j(\omega+\Omega-\omega_0)+\zeta} \\ &- \frac{k_1^+ k_1^+}{j(\omega+\Omega-\omega_0)+\zeta} - \frac{k_1^- k_1^+}{j(\omega+\Omega-\omega_0)+\zeta} \\ &- \frac{k_1^0 k_1^-}{j(\omega-\Omega-\omega_0)+\zeta} - \frac{k_1^+ k_1^-}{j(\omega-\Omega-\omega_0)+\zeta} \\ &- \frac{k_1^- k_1^-}{j(\omega-\Omega-\omega_0)+\zeta} \ . \end{aligned} \tag{2.28}$$

A similar procedure can be done to find that

$$\begin{aligned} S_{12} = e^{-j\beta\ell(N-1)} &- \frac{k_1^0 k_2^0}{j(\omega-\omega_0)+\zeta} - \frac{k_1^+ k_2^0}{j(\omega-\omega_0)+\zeta} \\ &- \frac{k_1^- k_2^0}{j(\omega-\omega_0)+\zeta} - \frac{k_1^0 k_2^+}{j(\omega+\Omega-\omega_0)+\zeta} \\ &- \frac{k_1^+ k_2^+}{j(\omega+\Omega-\omega_0)+\zeta} - \frac{k_1^- k_2^+}{j(\omega+\Omega-\omega_0)+\zeta} \\ &- \frac{k_1^0 k_2^-}{j(\omega-\Omega-\omega_0)+\zeta} - \frac{k_1^+ k_2^-}{j(\omega-\Omega-\omega_0)+\zeta} \\ &- \frac{k_1^- k_2^-}{j(\omega-\Omega-\omega_0)+\zeta} \ , \end{aligned} \tag{2.29}$$

and

$$\begin{aligned} S_{22} = e^{-j\beta\ell(N-1)} &- \frac{k_1^0 k_1^0}{j(\omega-\omega_0)+\zeta} - \frac{k_1^+ k_1^0}{j(\omega-\omega_0)+\zeta} \\ &- \frac{k_1^- k_1^0}{j(\omega-\omega_0)+\zeta} - \frac{k_1^0 k_1^+}{j(\omega+\Omega-\omega_0)+\zeta} \\ &- \frac{k_1^+ k_1^+}{j(\omega+\Omega-\omega_0)+\zeta} - \frac{k_1^- k_1^+}{j(\omega+\Omega-\omega_0)+\zeta} \\ &- \frac{k_1^0 k_1^-}{j(\omega-\Omega-\omega_0)+\zeta} - \frac{k_1^+ k_1^-}{j(\omega-\Omega-\omega_0)+\zeta} \\ &- \frac{k_1^- k_1^-}{j(\omega-\Omega-\omega_0)+\zeta} \ . \end{aligned} \tag{2.30}$$

Recall that the coupling constants $k_m^{\pm}$ contain $e^{j\pm\Omega}$ terms, which are frequency shifts of $\pm\Omega$. Thus, the scattering matrix has several components that can be separated by the frequency shift they impose. The linear transfer functions, with no frequency shift, are

$$\begin{aligned} S_{21} = e^{-j\beta\ell(N-1)} &- \frac{k_2^0 k_1^0}{j(\omega-\omega_0)+\zeta} - \frac{k_2^- k_1^+}{j(\omega+\Omega-\omega_0)+\zeta} \\ &- \frac{k_2^+ k_1^-}{j(\omega-\Omega-\omega_0)+\zeta} \ , \end{aligned} \tag{2.31}$$

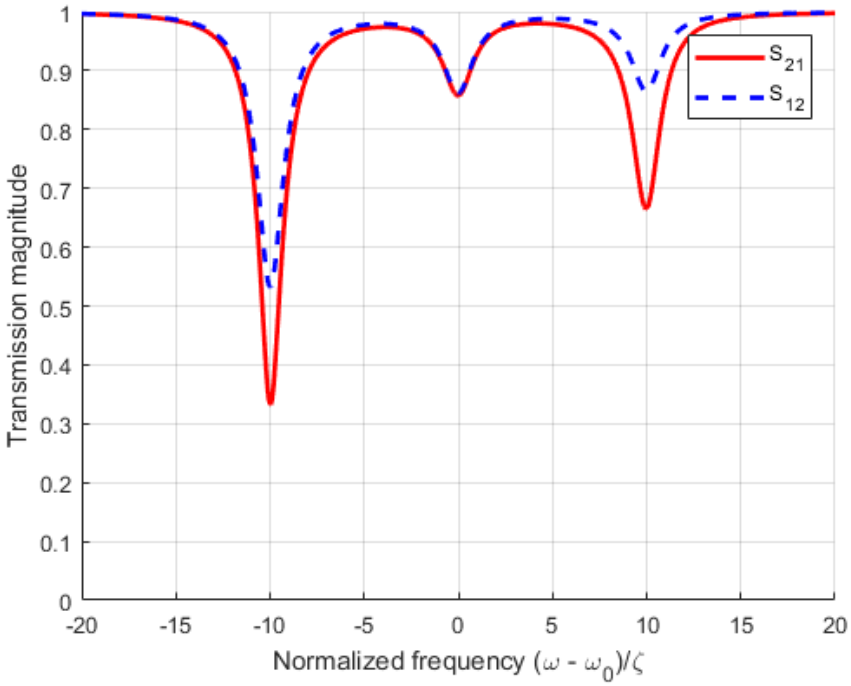

Figure 2.3: Example transmission calculated from Equations (2.31) and (2.32). The coupling parameters used in these calculations are shown in Table 2.1. The modulation frequency is $\Omega = 10\zeta$ and the intrinsic resonator loss is $\kappa = (1/15)\zeta$.

and

$$S_{12} = e^{-j\beta\ell(N-1)} - \frac{k_1^0 k_2^0}{j(\omega-\omega_0)+\zeta} - \frac{k_1^- k_2^+}{j(\omega+\Omega-\omega_0)+\zeta} - \frac{k_1^+ k_2^-}{j(\omega-\Omega-\omega_0)+\zeta} \,. \tag{2.32}$$

In the paths composing these linear transfer functions there is either no frequency shift (in the first term) or two cancelling frequency shifts (in the second and third terms). The linear transfer function, with no overall frequency shift, is typically the most important piece of the total transfer function, since unwanted terms that are frequency shifted can be filtered out by a band-stop (band-reject) filter.

From the above equations and Fig. 2.3 we find that the synthetic phonon enabled

Table 2.1: Coupling parameters used to calculate the transmission spectra shown in Fig. 2.3. The sum of the coupling rates $2\gamma = (28/15)\zeta$ such that $\gamma = (14/15)\zeta$.

	Center frequency	Stokes sideband	Anti-Stokes sideband
S_{21}	$k_2^0 k_1^0 = (2/15)\zeta$	$k_2^- k_1^+ = (2/3)\zeta$	$k_2^+ k_1^- = (1/3)\zeta$
S_{12}	$k_2^0 k_1^0 = (2/15)\zeta$	$k_1^- k_2^+ = (7/15)\zeta$	$k_1^+ k_2^- = (2/15)\zeta$

coupling results in a distinct transmission spectrum where resonant absorption can occur at the original resonance frequency, ω_0, as well as the shifted frequencies $\omega_0 \pm \Omega$. In the rest of this thesis, the absorption at $\omega_0 - \Omega$ is referred to as the Stokes sideband and the absorption at $\omega_0 + \Omega$ as the anti-Stokes sideband (see Fig. 2.2b). Since $k_1^+ \neq k_1^-$ and $k_2^+ \neq k_2^-$ (from Equations (2.18) and (2.19)), transmission at the sideband frequencies can be strongly nonreciprocal due greater resonant absorption for one direction at each sideband. As an example, the spectrum of the calculated linear transfer functions S_{21} and S_{12} are shown in Fig. 2.3 with the parameters listed in Table 2.1. The transmission spectrum is clearly nonreciprocal at the sideband frequencies, where the nonreciprocal coupling occurs. Note that, as in Fig. 2.3, absorption at the sidebands is in general asymmetric due to the frequency dependence of $k_{1,2}$ that results from the frequency dependence of β.

Chapter 3

Nonreciprocal coupling: Experiment

This chapter presents experimental evidence of nonreciprocal coupling in microstrip circuits. First, it reviews the theory of resonators and waveguides in microstrip circuits and discusses technical details important to understanding modulated coupling between such waveguides and resonators. It next showcases experimental data which demonstrates nonreciprocal coupling to microstrip resonators and experimental confirmation of the theory of operation from Chapter 2.

3.1 Microstrip circuits: Waveguides and resonators

Modeling electromagnetic waves traveling at a finite speed is vital to the study of waveguides and resonators. Conventional circuit theory assumes that the physical dimensions of a circuit are much smaller than the wavelength, so that all parts of the circuit can be considered in-phase for a given time-varying signal. Transmission line theory extends circuit theory to account for the travel time in circuits that cannot be approximated in this way. A detailed analysis of transmission lines can be found in Ref. [5].

Conventional circuit theory can be used to model small pieces of a transmission line with length Δz, as shown in Fig. 3.1. The transmission line is modeled as having a series resistance per unit length R, a series inductance per unit length L, a shunt conductance per unit length G, and a shunt capacitance per unit length C. Applying Kirchoff's laws to this circuit model leads to the differential equations for

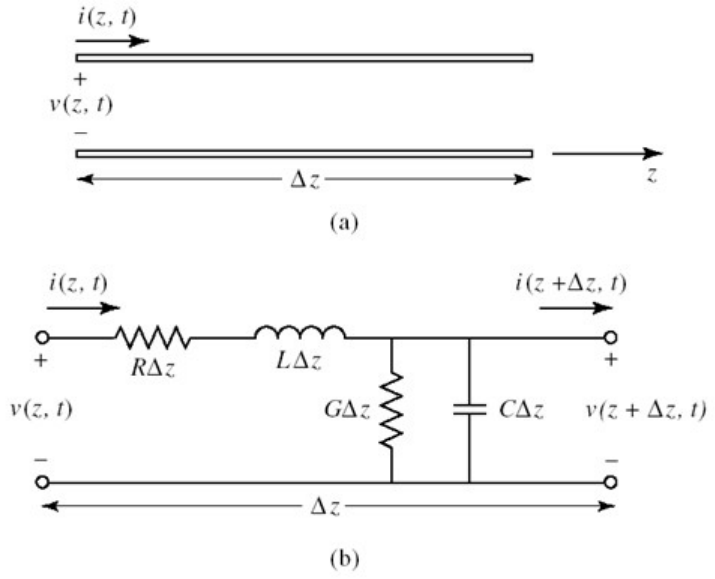

Figure 3.1: Voltage and current definitions and equivalent circuit for an incremental length of transmission line. (a) Voltage and current definitions. (b) Lumped element equivalent circuit. From Ref. [5].

the voltage and current

$$\frac{dV(z)}{dz} = -(R + j\omega L)I(z) \ , \tag{3.1}$$

$$\frac{dI(z)}{dz} = -(G + j\omega C)V(z) \ , \tag{3.2}$$

using phasor notation with a frequency of ω. Equations (3.1) and (3.2) are known as the *telegrapher equations*.

The solutions to these equations take the form of traveling waves

$$V(z) = V_0^+ e^{-\gamma z} + V_0^- e^{\gamma z} \ , \tag{3.3}$$

$$I(z) = I_0^+ e^{-\gamma z} + V_0^- e^{\gamma z} \ , \tag{3.4}$$

where the $e^{-\gamma z}$ terms represent waves traveling in the $+z$ direction, and the other term waves traveling in the $-z$ direction. The propagation constant γ can be defined in terms of the circuit parameters as

$$\gamma = \sqrt{(R + j\omega L)(G + j\omega C)} \ . \tag{3.5}$$

The amplitude of the voltage and current waves are related by the characteristic impedance Z_0 of the transmission line,

$$\frac{V_0^+}{I_0^+} = \frac{V_0^-}{I_0} = Z_0 \ . \tag{3.6}$$

The characteristic impedance Z_0 can also be defined in terms of the circuit parameters,

$$Z_0 = \sqrt{\frac{R + j\omega L}{G + j\omega C}} \ . \tag{3.7}$$

If loss in the transmission line is small, the line can be approximated as lossless by setting $R = G = 0$. In this case the propagation constant reduces to $\gamma = j\beta = j\omega\sqrt{LC}$, and the characteristic impedance to $Z_0 = \sqrt{\frac{L}{C}}$. Note that this is the same propagation constant that was assumed in the waveguide in the previous section. In

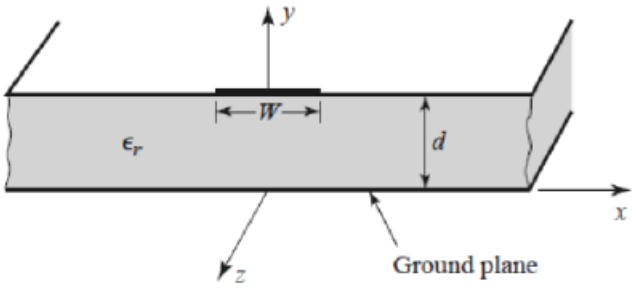

Figure 3.2: Microstrip transmission line geometry. From Ref. [5].

fact, transmission lines are (loosely) the same thing as waveguides.

Microstrip transmission lines are a very widely used type of planar transmission line, mainly because they can be fabricated and integrated with other microwave devices easily [5]. A cross section of a microstrip line is shown in Fig. 3.2, it consists of a conductive ground plane, a dielectric (insulator) of height d with dielectric constant ϵ_r, and a top conductor of width W. The geometry of the top conductor, which can take any shape desired, defines the microstrip line. For example, the top conductor can be pattern in a thin straight line to form a waveguide, in a fan shape [54] or spiral [55] to form a compact filter, or in a multitude of different shapes to produce more complex behaviors. Surface mount components, including resistors, capacitors, and diodes, can be soldered to the top conductor to connect these devices to the microstrip transmission line. The top conductor or any surface mount component can be shorted directly to the ground plane through a *via*, a hole in the substrate lined with conductive material.

The propagation constant β of a microstrip transmission line can be expressed as

$$\beta = \frac{\omega}{c}\sqrt{\epsilon_e}\ , \tag{3.8}$$

where c is the speed of light in a vacuum. The effective dielectric constant ϵ_e is related to the dielectric constant ϵ_r of the insulator substrate used to build the microstrip line by a complex relationship that depends on the substrate thickness d, the conductor width W, and the frequency of operation. These effects can be modeled analytically

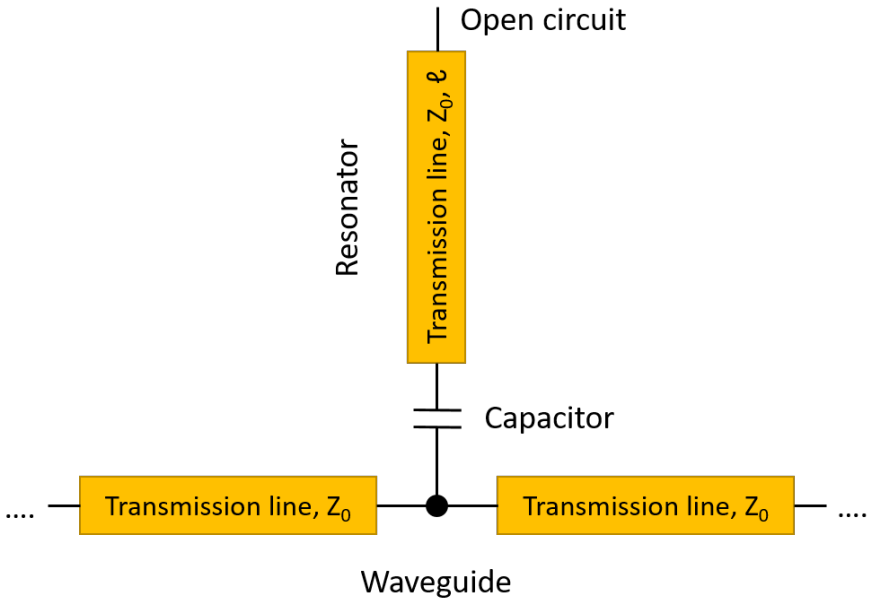

Figure 3.3: Transmission line diagram of a waveguide-resonator circuit.

or simulated using computer software to find the effective dielectric constant. The impedance of the microstrip line also depends on several parameters and can either be solved for analytically or using a software simulation. Modern simulations are quite accurate and give results that match very closely with experimental results, especially at lower frequencies (< 10 GHz), making microstrip a convenient technology for accurate experimental implementation of transmission line circuits.

Using conventional transmission line theory, it can easily be shown how resonators can be constructed from transmission lines, including microstrip transmission lines. A diagram of a simple transmission line resonator coupled to a waveguide is shown in Fig. 3.3. It consists of an open-circuited transmission line stub, coupled in parallel through a capacitor to a series of transmission lines that form a waveguide.

The input impedance of a transmission line characterizes the voltage-current relationship at a point a specific distance away from a load that terminates the line. For a lossless line, the input impedance at a distance ℓ from a load with impedance

Z_L is defined as [5]

$$Z_{\text{in}} = Z_0 \frac{Z_L + jZ_0 \tan(\beta\ell)}{Z_0 + jZ_L \tan(\beta\ell)} \ . \tag{3.9}$$

If the transmission line is terminated in an open circuit such that $Z_L \to \infty$ (as in Fig. 3.3), forming an open-circuited stub, this reduces to

$$Z_{\text{in}} = -jZ_0 \cot(\beta\ell) \ . \tag{3.10}$$

As will be demonstrated shortly, this stub behaves as a resonator if it is weakly coupled (through a small capacitance or large inductance) to another circuit. The resonance frequencies of the stub resonator are located at the frequencies where the relation $\beta\ell = (2n+1)\pi$, where n is an integer, is satisfied. Since $\beta\ell$ is approximately linearly dependent on frequency, there will always exist a number of frequencies for which the open-circuited stub resonates. The lowest of these frequencies, where $\beta\ell = \pi$ (or $n = 0$), is the fundamental resonance of the stub.

The stub resonator can be coupled to a waveguide through a small capacitance. The impedance of a capacitor is given by

$$Z_{\text{cap}} = \frac{1}{j\omega C} \ . \tag{3.11}$$

The capacitor is connected to the stub resonator in series, resulting in an overall impedance

$$Z_{\text{res}} = Z_{\text{cap}} + Z_{\text{in}} = \frac{1}{j\omega C} - jZ_0 \cot(\beta\ell) \ . \tag{3.12}$$

To connect this resonator to a waveguide, we can place it as a shunt admittance in parallel with a transmission line, where the shunt admittance is defined as

$$Y_{\text{res}} = \frac{1}{Z_{\text{res}}} \ . \tag{3.13}$$

The transmission through the waveguide with this shunt admittance in parallel is given by [5]

$$S_{21} = S_{12} = \frac{2}{2 + Y_{\text{res}} Z_0} \ , \tag{3.14}$$

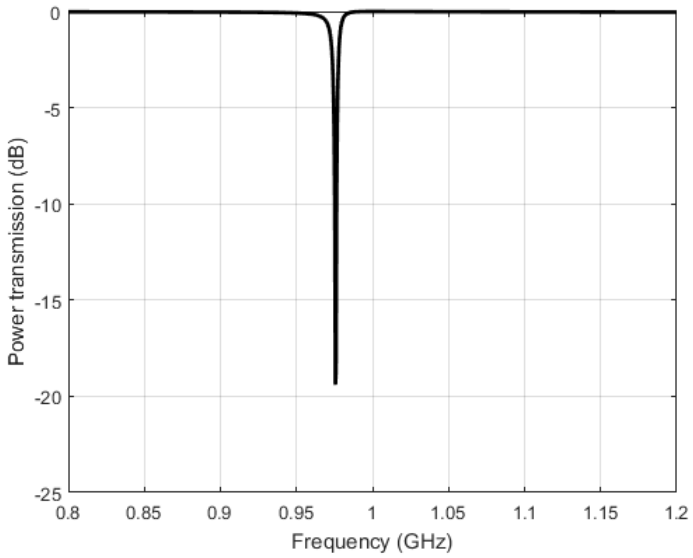

Figure 3.4: Calculated transmission through a waveguide with characteristic impedance $Z_0 = 50\ \Omega$ coupled to a stub resonator of length $\beta\ell = \pi$ at the resonance frequency $f_0 = \omega_0/2\pi = 1$ GHz. The resonator and waveguide are coupled through a capacitor with $C = 0.5$ pF. All transmission line theory calculations were performed using MATLAB [56].

where Z_0 is the characteristic impedance of the *waveguide* transmission line, not the *resonator* transmission line as in Eq. (3.10). Of course, often the resonator and waveguide are created from the same transmission line and have the same characteristic impedance. An example of the calculated power transmission spectrum for this system, $20\log_{10}|S_{21}|$, is shown in Fig. 3.4. The spectrum clearly shows the typical response of a resonator, a sharp dip in transmission.

The transmission line resonator system can be modeled using coupled-mode theory as discussed in Chapter 2. As derived in the previous chapter, the canonical equation for transmission through a waveguide that is side-coupled to a lossless resonator (such that the resonator behaves as a shunt admittance) is

$$S_{21} = 1 - \frac{\gamma}{j(\omega - \omega_0) + \gamma}\ , \tag{3.15}$$

where γ is the coupling rate between the waveguide and resonator and ω_0 is the resonator's resonance frequency. A zoomed-in version of Fig. 3.4 is shown in comparison to the coupled-mode theory model in Fig. 3.5. The two models match reasonable well, although there is some slight asymmetry in the spectrum of the transmission line model that is not present in the coupled-mode theory model. Especially for low coupling rates (if the capacitor impedance $C_{\text{cap}} \geq Z_0$), the coupled-mode theory model of a resonator provides a good approximation of the more exact transmission line model. From this analysis, we can see that microstrip transmission lines provide a viable platform for experimentally testing the theory developed in Chapter 2. Microstrip transmission lines can be used to produce both waveguides and resonators, and capacitors can be used to couple these together. The next section will discuss in detail how coupled-mode theory applies to microstrip resonator circuits and where deviations from the theory occur.

3.2 Transmission line resonators and coupled-mode theory

Coupled-mode theory can be used to model the interactions between transmission line waveguides and resonators. However, there are several approximations made in coupled-mode theory that can break down in commonly encountered situations when using microstrip resonator circuits. The model used in Chapter 2, which simply injects time-varying coupling rates, is over-simplified and not sufficiently accurate to design working circuits. This section will discuss some of the deviations from coupled-mode theory that are encountered in the design of microstrip circuits that exhibit strong nonreciprocal coupling.

An extremely illustrative example of where the coupled-mode theory approximations break down is shown in Fig. 3.6. This figure displays six transmission spectra for the simple waveguide resonator circuit in Fig. 3.3. Each subplot (a-f) differs only in the coupling capacitance. For a small capacitance of 0.5 pF or less (Fig. 3.6a, also Fig. 3.5) the transmission line resonator is well-modeled by coupled-mode theory and the transmission spectrum is approximately symmetric. However, as the

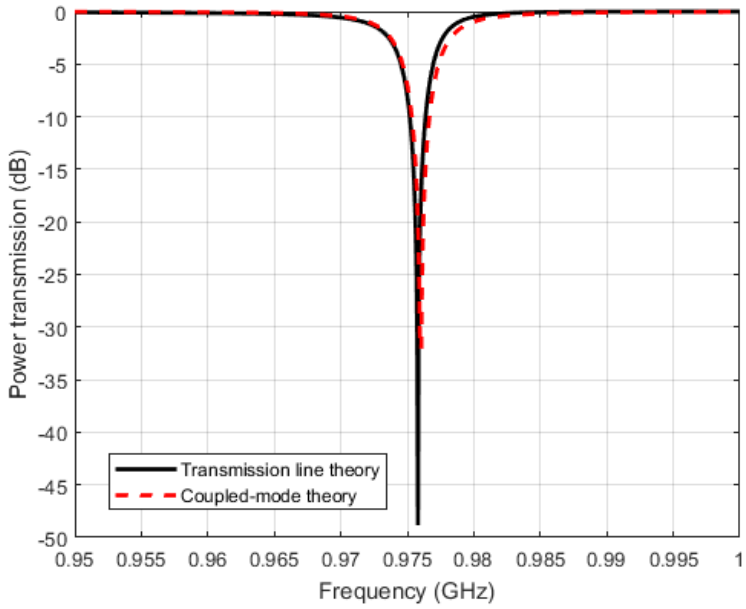

Figure 3.5: Calculated transmission for a waveguide side-coupled to a resonator. Black line corresponds to the transmission line theory (Fig. 3.4), red line corresponds to coupled-mode theory fit. Transmission dip is deeper than in Fig. 3.4 due to the increased resolution — since this is a lossless resonator transmission is exactly 0 ($-\infty$ dB) at the resonance frequency.

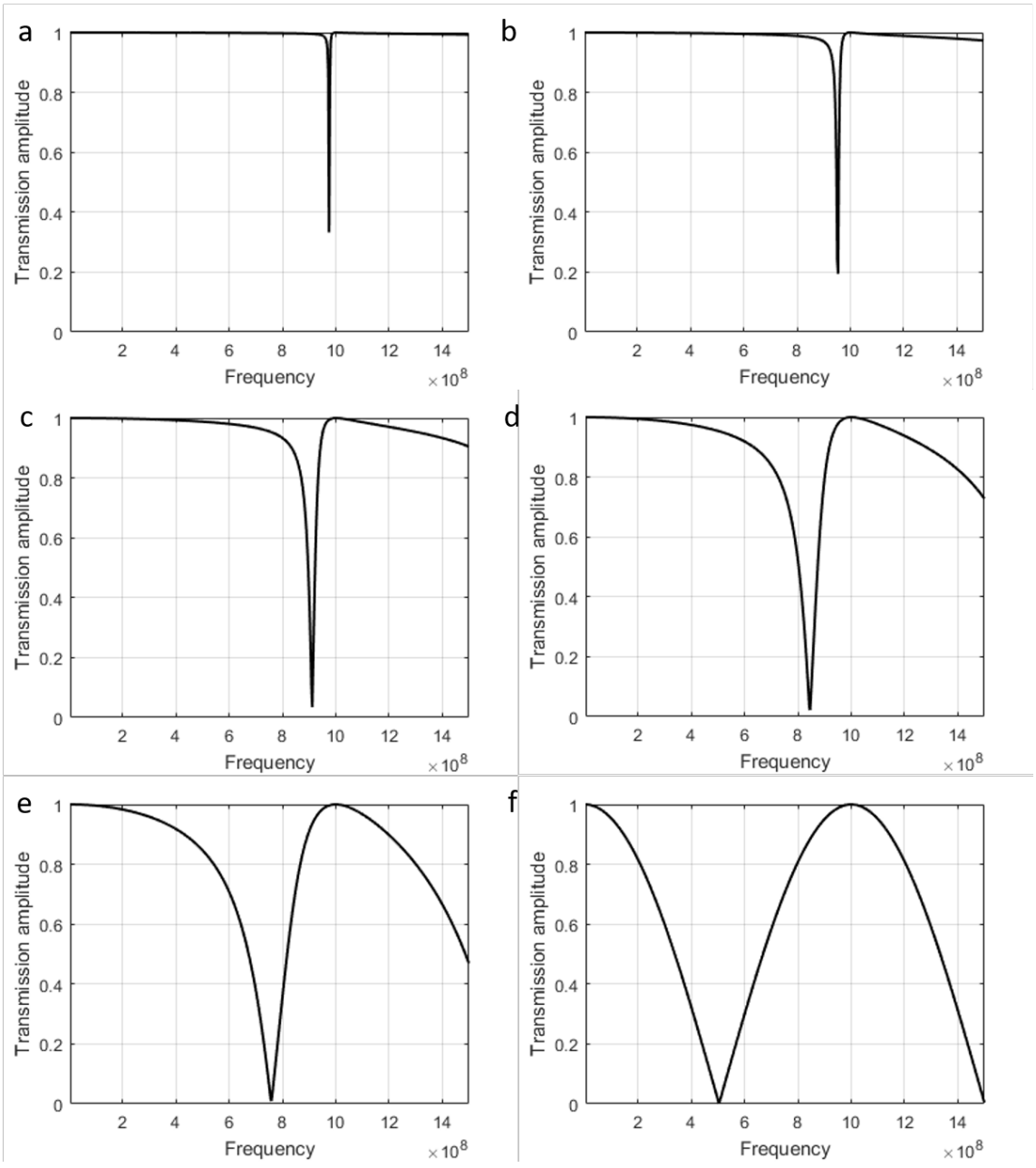

Figure 3.6: Calculated transmission through a transmission line waveguide coupled to a transmission line resonator with fundamental resonance frequency $f_0 = 1$ GHz. The waveguide and resonator are coupled with through a: (a) 0.5 pF capacitor, (b) 1 pF capacitor, (c) 2 pF capacitor, (d) 4 pF capacitor, (e) 8 pF capacitor, (f) 1000 pF capacitor.

coupling capacitance increases (b-e), the transmission spectrum becomes more and more asymmetric and the coupled-mode theory model becomes less accurate.

There are several features that illuminate why the spectrum is asymmetric. First, note that transmission at the resonance frequency (1 GHz) is always unity. This is counter-intuitive since normal resonators resonate at their resonance frequency, i.e. the resonance frequency is typically where the highest absorption occurs. However, Eq. (3.12) shows that the resonator impedance goes to ∞ at the resonance frequency, thus no energy can enter the resonator and no absorption can occur. In general, the transmission line resonator impedance varies with frequency. This property also affects how frequency-shifted coupling behaves, as will be discussed later in this section.

The other feature of Fig. 3.6 is the transmission spectrum as the coupling capacitance $C \to \infty$, shown in subplot (f). Here the spectrum has a purely sinusoidal shape, in contrast to the Lorentzian for a low coupling capacitance. In this limit, the capacitance behaves as a short circuit (with $Z_{\text{cap}} = 0$) so that the response of the resonator is the same as an open-circuited stub. The interplay between the sinusoidal response at very high capacitance and Lorentzian at very low capacitance, which is well modeled by coupled-mode theory, determines the transmission spectrum of the transmission line resonator.

Now consider the same simple transmission line resonator circuit, but the capacitance can vary with time. First, we can examine how adiabatic changes in the capacitance affect the overall transfer function. Figure 3.7 shows a comparison of two transmission spectra. The left transmission spectrum is from the canonical transmission line resonator circuit with 0.9 pF coupling capacitance (black) with a coupled-mode theory fit using the coupled-mode theory equation (red, dashed)

$$S_{21} = 1 - \frac{\gamma}{j(\omega - \omega_0) + \zeta} \ , \tag{3.16}$$

where $\zeta = \gamma + \kappa$ and κ is the intrinsic loss rate of the resonator. A small amount of loss is added to the transmission line resonator such that the peak absorption

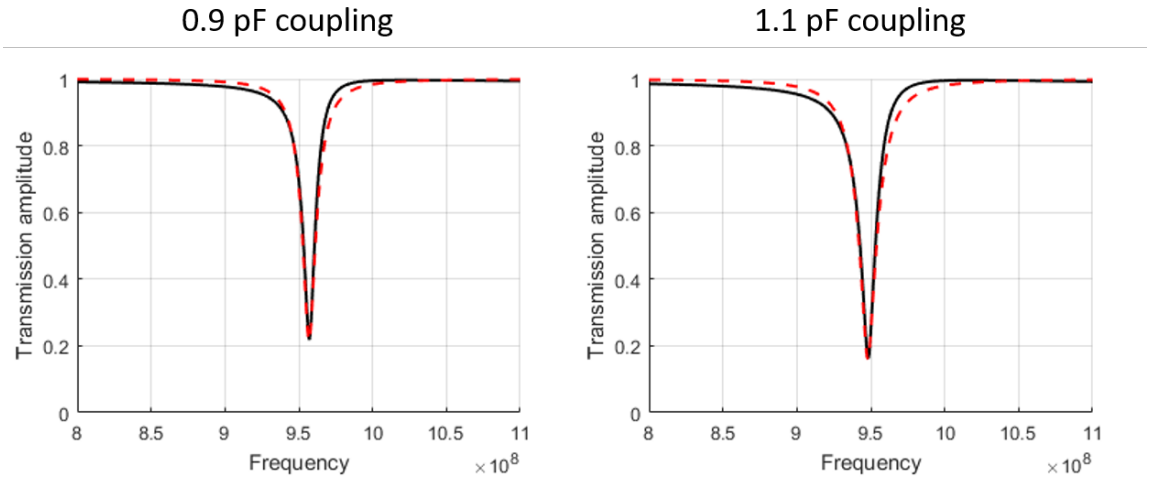

Figure 3.7: Comparison of transmission spectrum of two transmission line waveguide-resonator circuits (black) with coupled-mode theory fits (red, dashed). The two transmission line circuits vary only in the coupling capacitance.

increases with an increasing coupling rate. The right transmission spectrum is from an identical circuit but with a 1.1 pF coupling capacitance (black) with a similar coupled-mode theory fit.

By inspecting these graphs, we can see that increases in the coupling capacitance lead to both a negative frequency shift, an increase in the peak absorption, and an increase in the linewidth. The frequency shift occurs because the coupling capacitance effectively loads the transmission line, increasing its electrical length (and thus shifting the frequency down). This effect is not modeled in coupled-mode theory as it has been presented, and must be added in explictly. The latter two of these three are well modeled by coupled-mode theory, since by increasing γ in Eq. (3.16) both the peak absorption and linewidth increases.

Table 3.1: Fitting parameters used in Fig. 3.7.

	0.9 pF	1.1 pF
$f_0 = \omega_0/(2\pi)$	957 MHz	948 MHz
γ	6.3 MHz	9.0 MHz
κ	1.7 MHz	1.7 MHz

The parameters for the coupled-mode theory fits in Fig. 3.7 are given in Table 3.1. Focusing on the coupling parameter γ, we find the relation

$$\left(\frac{0.9}{1.1}\right)^2 \approx \frac{6.3}{9} \ , \tag{3.17}$$

where the left-hand side is the coupling capacitance ratio squared, and the right-hand side is the γ relation between the two graphs. These are approximately equal (the fit is not perfect so there is some discrepancy), meaning that a small change in capacitance can be modeled as a linear change in the coupling constant, which is related to $\sqrt{\gamma}$. This analysis shows that a modulated coupling constant as introduced in Chapter 2 can be implemented in an experimental system directly as a modulated capacitance.

The derivation of nonreciprocal coupling presented in Chapter 2 assumes that the frequency of modulation Ω is much larger than the linewidth ζ, the resolved sideband regime. The resolved sideband regime only occurs in non-adiabatic systems, and non-adiabatic changes in the coupling capacitance produce a very different transmission spectrum than the adiabatic changes in capacitance described above. The simplest system that we can analyze is the same canonical transmission line resonator circuit as before, but with a coupling capacitance that varies rapidly. This problem is difficult to solve using standard transmission line theory, but is simple to produce experimentally.

To perform this experiment, a transmission line resonator circuit with a single variable capacitor was implemented using microstrip circuits and varactor diodes. Details on the implementation are discussed in the next section. The transmitted power was measured at the original incidence frequency and the first-order sidebands at $\omega \pm \Omega$ when the coupling capacitance was sinusoidally modulated at 100 MHz. The results are shown in Fig. 3.8. The black data points correspond to the transmitted power without a frequency shift, and clearly show the resonant absorption response. The resonance frequency of this circuit is 1.4 GHz due to capacitive loading, while the unloaded resonance frequency (the point of infinite impedance) is ≈ 1.65 GHz.

The orange and blue data points correspond to the transmitted power at $\omega + \Omega$ and $\omega - \Omega$ respectively. The main result of this experiment is the asymmetric frequency response: below the resonance frequency both the up- and down- shifted transmission is approximately equal, while above it they are drastically different. At the resonance frequency of 1.4 GHz there is a clear peak in the up-shifted transmission that corresponds to incidence at 1.3 GHz and inelastic scattering into the resonance. However, there is no clear peak in the down-shifted transmission for the same process - *why is this*?

We know from the transmission line analysis that the impedance of the resonator is infinite at the unloaded resonance frequency (here 1.65 GHz) and lowest where the largest absorption occurs (1.4 GHz). However, below the absorption peak the resonator impedance does not rise rapidly, instead it remains fairly low. In fact, it can be seen from the transmission line analysis that at half the unloaded resonance frequency the stub impedance is 0 and the entire resonator system behaves as a capacitor short-circuited to ground. Thus, we can understand the discrepancy in the modulated scattering as a result of the resonator impedance: above the absorption peak the impedance rises rapidly and inelastic scattering to and from these frequencies is suppressed, while below it the impedance remains low and scattering is permitted. In the limit where the resonator impedance goes to infinity, at 1.65 GHz, there can be no scattering at all from the modulated capacitance. This limit can be understood easily: since impedance of a capacitor in series with an open circuit (infinite impedance) is always infinite, modulating the capacitance has no effect.

From the above analysis we can conclude several important points that have a major impact on the experimental implementation of nonreciprocal coupling. First, the capacitance of the coupling capacitor has a major influence on the frequency of the resulting resonator. While this would in theory mean that modulating the capacitance would also modulate the resonance frequency, this problem is automatically overcome by using three or more coupling capacitors (coupling sites) that are phased such that the total capacitance does not change in time. Since the loading depends only on the summed total of all coupling capacitors (if they are connected to the same point on the resonator), these modulation schemes result in an unmod-

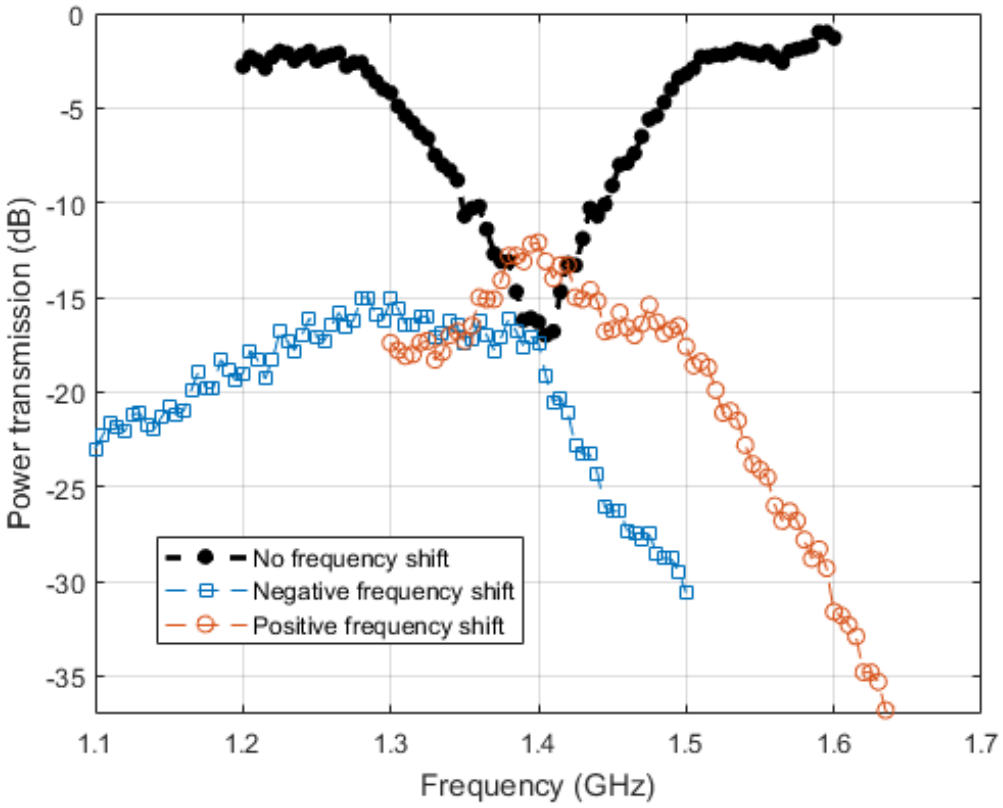

Figure 3.8: Power transmission through a microstrip resonator circuit with a coupling capacitor modulated at 100 MHz. Black dots are measured power transmission with no frequency shift, showing the absorption curve of the resonator. Blue and orange points are the measured power transmission with a $\pm$100 MHz frequency shift. The x-axis frequency is the output frequency, including the frequency shift.

ulated resonance frequency. Second, the coupling constant used in coupled-mode theory is linearly proportional to the capacitance of the coupling capacitor between a transmission line waveguide and resonator (assuming a small coupling capacitance). Time-varying capacitors can therefore be used experimentally to directly implement the time-varying coupling constants described the theory of nonreciprocal coupling in Chapter 2. Third, the effectiveness of the modulated coupling capacitor (at shifting the frequency of incoming waves as they couple into the resonator) is highly dependent on the resonator's impedance at both the incident frequency of the waves and the final frequency after scattering. The exact nature of this relationship is not easily understood, but in the limiting case of infinite resonator impedance at either frequency no scattering occurs at all.

Any circuit designed to experimentally realize nonreciprocal coupling must take this "modulation efficiency" into account. It may be possible to approximate the resonator impedance in more complex circuits, such as those with multiple coupling capacitors where the frequency (or frequencies) of high resonator impedance is not so easily found, by measuring the derivative of the transmission amplitude with small changes in the coupling capacitance. While this is somewhat of a heuristic, it is based in sound arguments and is useful for the design of circuits that implement nonreciprocal coupling. If the transmission amplitude does not change much with changes in coupling capacitance, it means that the capacitor does not affect the waves in the waveguide much, and a high resonator impedance and therefore low modulation efficiency can be assumed. In contrast, if the transmission amplitude changes significantly it means that the capacitor has a large effect on waves in the waveguide and a high modulation efficiency can be assumed. The circuits used in the experiments described in the remainder of this chapter and in Chapter 4 were designed with these principles in mind.

3.3 Nonreciprocal coupling in microstrip circuits

All experimental microwave circuits in this thesis are fabricated on Rogers RT/duroid 5880 or RT/duroid 6006 substrate with a 1 oz copper conductor, and consist of a microstrip waveguide coupled to a stub or ring resonator by N varactor diodes (Skyworks SMV1275) that act as variable capacitors. The coupling strength c_n of each capacitive coupler is an approximately linear function of the applied voltage V_n (for small changes), allowing a modulation of c_n that is proportional to a modulation of V_n. A DC bias is applied to each varactor diode with a DC power supply (Agilent E3631A), which lowers the capacitance and decreases the background reflection caused by the coupling system. On top of this bias, small sinusoidal signal is applied from a signal generator (HP-8647B). This signal is split (Minicircuits ZA3CS-400-3W-S) into three variable phase shifters (Minicircuits JSPHS-150+) so that the phase shift between each signal can be independently controlled. The DC bias and three 104 MHz modulation signals are combined through a three bias tees (Minicircuits ZFBT-4R2GW-FT+) and connected directly to the circuit, e.g. through the ports labeled *Bias* in Fig. 3.9. On each circuit, butterfly band-pass filters were incorporated along with a another low-frequency biasing tee (Johanson Technology L-14C10N-V4T 10 nH inductor and Johanson Technology R14S 6.8 pF capacitor) as shown in Fig. 3.9 to isolate the lower-frequency (104 MHz) bias modulation from the higher-frequency (≈ 1.4 GHz) resonant circuit.

To experimentally validate the theory of nonreciprocal coupling, a waveguide-resonator system with three coupling sites ($N = 3$) was implemented using a microstrip waveguide and stub resonator (Fig. 3.9, right). The fabricated resonator has a loaded resonance frequency $\omega_0/2\pi \approx 1.4$ GHz. The waveguide and resonator are coupled through variable capacitors (varactor diodes), which allows dynamic control over the coupling constants c_n though an applied voltage. The coupling site separation is designed such that $\beta(\omega_0)\ell = 2\pi/3$, resulting in a complete phase mismatch and creating a dark state. Without a synthetic phonon bias, the measured transmission for this circuit (Fig. 3.9, left) does not indicate any dips corresponding to resonant absorption, confirming that interactions between the resonator and waveguide are

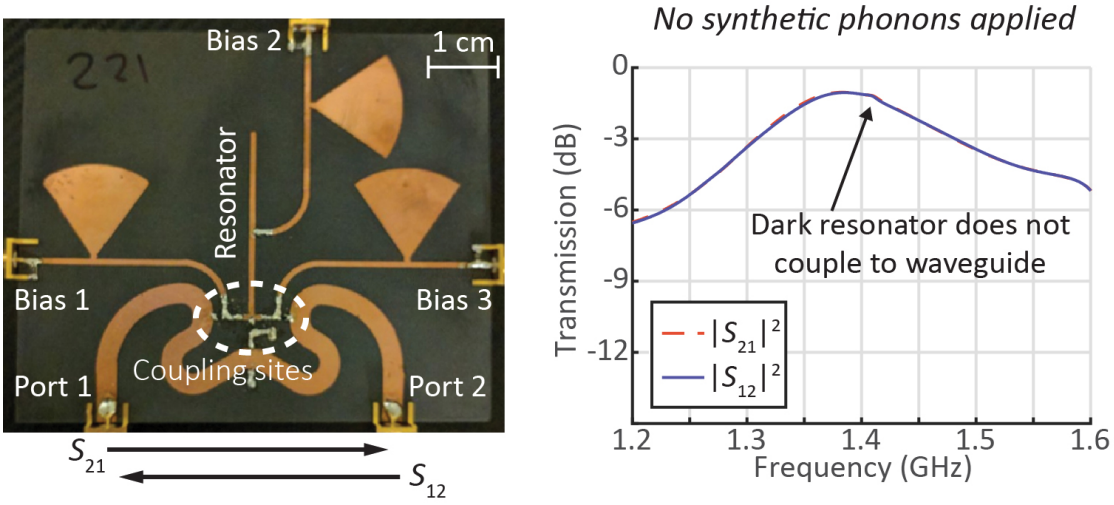

Figure 3.9: Experimental measurement of an engineered dark state. Picture of the experimental circuit (right, see Fig. 3.11d for the circuit diagram) and measured power transmission (left). The resonance does not interact with the waveguide (i.e. is *dark*) due to destructive interference from multiple coupling sites, and therefore no dip in transmission is observed.

suppressed by the phase mismatch. The broadband background transmission losses are caused by a reflection from the capacitive coupling network, an effect that is not well modeled by temporal coupled-mode theory.

Synthetic phonons are applied to this circuit through an applied time-varying voltage. The synthetic phonons have frequency $\Omega/2\pi = 104$ MHz and momentum $q = -\beta(\omega_0 + \Omega)$, which is implemented through a phase offset $\theta_n = (5\pi/3)(n-1)$ as described by Eq. (2.17). This phonon momentum was empirically tuned to maximize the coupling rate $k_1^+ k_2^-$, between the resonator and backward waveguide mode at the anti-Stokes sideband. From Eq. (2.31), this coupling rate also describes coupling for the forward waveguide mode at the Stokes sideband (neglecting the frequency dependence), thus resonant absorption should occur nonreciprocally: at the anti-Stokes sideband for backward transmission and at the Stokes sideband for forward transmission. The coupling rate $k_2^+ k_1^-$ is simultaneously minimized by this choice of phonon momentum, so no absorption is expected at these frequencies for the

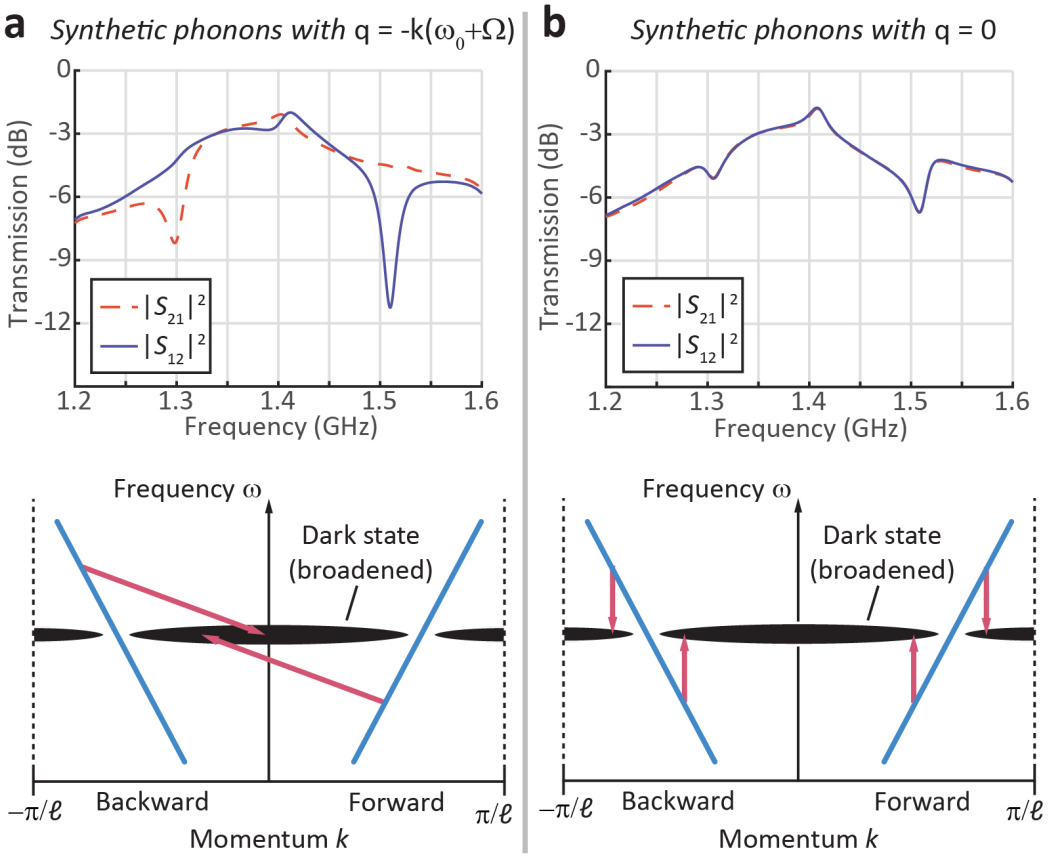

Figure 3.10: Experimentally measured nonreciprocal resonant absorption from synthetic-phonon enabled coupling between a microstrip waveguide and resonator. **b**, Synthetic phonons with the correct momentum are applied such that $-\beta(\omega_0 + \Omega) - q = 0$, facilitating nonreciprocal coupling to the resonator which manifests as a Stokes sideband for forward propagating photons (S_{21} measurement) and an anti-Stokes sideband for reverse propagating photons (S_{12} measurement). The resonance is broadened in momentum space due to the number of couplers ($N = 3$), which only completely destructively interfere for $\beta = \pm 2\pi/3\ell$. **c**, Synthetic phonons with zero momentum ($q = 0$) are applied. Although no momentum shift occurs, coupling is present at the sideband frequencies due to waveguide dispersion. The system is reciprocal because these phonons do not break time-reversal symmetry.

opposite directions (anti-Stokes for forward transmission and Stokes for backward transmission).

The measured forward (S_{21}) and backward (S_{12}) transmission coefficients for this system are shown in Fig. 3.10a. As predicted, resonant absorption occurs at ≈ 1.3 GHz only in the forward direction and at ≈ 1.5 GHz only in the backward direction. The frequency dependence of β creates a slight phase mismatch at the Stokes sideband, resulting in less absorption. The measured absorption (and therefore transmission) is highly nonreciprocal: no resonant absorption is observed at ≈ 1.3 GHz in the backward direction or at ≈ 1.5 GHz in the forward direction, validating that $k_1^- = k_2^+ \approx 0$.

This experiments demonstrates that interactions with synthetic phonons can facilitate coupling to dark states by modifying the original phase matching condition. Furthermore, it shows that phonon-assisted coupling results in nonreciprocal transmission if this modified phase matching condition is not satisfied for both directions simultaneously. Synthetic phonons that do not modify the phase matching condition, i.e. phonons with zero momentum ($q = 0$), can also enable coupling to a dark resonator due to the frequency dependence of k. This case, which is shown experimentally in Fig. 3.10b, demonstrates that both waveguide directions can couple to a dark state simultaneously. Note that because a partial phase mismatch remains, the coupling is weaker at the sidebands and absorption is reduced compared to Fig. 3.10a.

3.4 Experimental tests of momentum matching

This section focuses on experiments testing how the transmission amplitude, which is the inverse of the coupling rate, varies with the applied synthetic phonon momentum q. Nonreciprocal waveguide-resonator systems having $N = 2$ and $N = 3$ couplers were implemented using microstrip ring resonators [57], as shown in Fig.

3.11. Synthetic phonons of the form

$$c_n = c_0 + \delta_c \cos(\Omega t - q\ell(n-1)) \tag{3.18}$$

were introduced with tunable momentum

$$q = \frac{\theta_n}{\ell(n-1)} = \frac{\phi}{\ell} \ , \tag{3.19}$$

where θ_n is the phase factor of the modulation applied to the n^{th} coupling site and ϕ is the phase shift between adjacent θ_n: $\theta_n - \theta_{n-1} = \phi = q\ell$. In the following, the variable ϕ is used to quantify the synthetic phonon momentum.

Using ϕ instead of q the coupling equations, Equations (2.18) and (2.19), can be rewritten as

$$\begin{aligned} k_1 = & \overbrace{c_0 \sum_{n=1}^{N} e^{-j\beta\ell(n-1)}}^{k_1^0} + \overbrace{\frac{c_M}{2} e^{j\Omega t} \sum_{n=1}^{N} e^{-j(\beta\ell+\phi)(n-1)}}^{k_1^+} \\ & + \overbrace{\frac{c_M}{2} e^{j\Omega t} \sum_{n=1}^{N} e^{-j(\beta\ell-\phi)(n-1)}}^{k_1^-} \ , \end{aligned} \tag{3.20}$$

$$\begin{aligned} k_2 = & \overbrace{c_0 \sum_{n=1}^{N} e^{j\beta\ell(n-1)}}^{k_2^0} + \overbrace{\frac{c_M}{2} e^{j\Omega t} \sum_{n=1}^{N} e^{j(\beta\ell-\phi)(n-1)}}^{k_2^+} \\ & + \overbrace{\frac{c_M}{2} e^{-j\Omega t} \sum_{n=1}^{N} e^{j(\beta\ell+\phi)(n-1)}}^{k_2^-} \ . \end{aligned} \tag{3.21}$$

With this new definition, it becomes clear that the coupling rate is determined by the phase shift $\beta\ell$ at the central band and $\beta\ell \pm \phi$ at the sidebands. By measuring the coupling rate at various ϕ, we can test this theoretical prediction of how the

nonreciprocal coupling arises. Additionally, by looking for the ϕ which minimizes the total coupling rate, we can measure the waveguide-induced phase shift $\beta\ell$.

The fabricated resonator system with two couplers ($N = 2$) shown in Fig. 3.11a,b has a loaded resonance frequency $\omega_0/2\pi \approx 1.57$ GHz. Figure 3.12a shows the measured Stokes and anti-Stokes transmission sidebands in forward and reverse directions when $\Omega/2\pi = 100$ MHz modulation is applied to the couplers, with relative phase setting of $\phi = 0$ (dashed lines) and $\phi = \pi/2$ (solid lines). The measured transmission at the Stokes sideband (frequency $\omega_0 - \Omega$) and anti-Stokes sideband resonance ($\omega_0 + \Omega$) as ϕ is swept from $-\pi$ to π are shown in Figure 3.12b,c respectively. As predicted, reciprocal transmission is observed at both $\phi = 0,\ \pi$. However, when ϕ is not equal to an integer multiple of π the coupling in the sidebands diverges depending on wave directionality, resulting in appreciable nonreciprocal transmission. In the Stokes sideband there is minimum forward coupling at $\phi = \pi/2$ and minimum reverse coupling at $\phi = -\pi/2$, confirming that the fabricated circuit has $\beta\ell = \pi/2$ at the Stokes sideband $\omega = \omega_0 - \Omega$. On the other hand, anti-Stokes sideband coupling is minimized at $\phi \approx \pm\pi/6$ (positive sign corresponds to minimized forward coupling) indicating that $\beta\ell = 7\pi/6$ at $\omega = \omega_0 + \Omega$. The large difference in $\beta\ell$ for these two frequencies can be attributed to the dispersion characteristics of the waveguide which are non-negligible in this experiment. Due to undesired additional resonant modes (which arise due to the symmetry of the ring resonator) and reflections in the circuit implementation the anti-Stokes sideband is much smaller and misshapen compared to the Stokes sideband. Despite these experimental difficulties, strong nonreciprocal coupling and over 5 dB of directional contrast is observed in this experiment.

The circuit with three coupling points ($N = 3$) has a loaded resonance frequency $\omega_0/2\pi \approx 1.41$ GHz and is shown in Fig. 3.11c,d. The Stokes and anti-Stokes sideband measurements for $\phi = 0$ (dashed lines) and $\phi = \pi/3$ (solid lines) are shown in Fig. 3.13a for an applied modulation frequency of $\Omega/2\pi = 100$ MHz. The measured transmission at the Stokes and anti-Stokes sideband resonances as ϕ is swept from $-\pi$ to π are shown in Fig. 3.13b,c. The three coupler case yields two distinct dips in transmission (one large, one small) as the phase setting ϕ is varied. These two dips in transmission correspond to two local maximums which occur in the sum of three

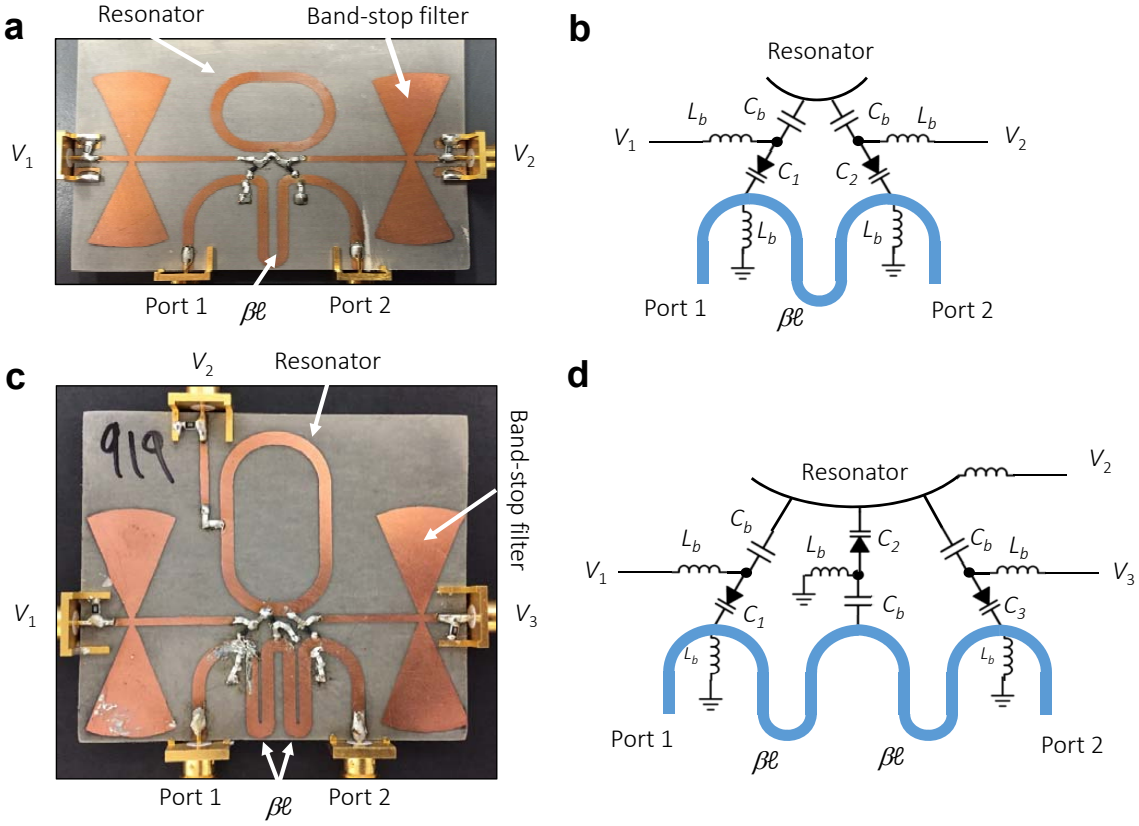

Figure 3.11: Microwave demonstration circuits for reconfigurable nonreciprocal coupling. (a,b) Photograph and schematic of a system with $N = 2$ coupling points. (c,d) Photograph and schematic of a system with $N = 3$ coupling points. Each microstrip ring resonator is coupled to the waveguide through multiple varactor diodes that are separated on the waveguide by phase $\beta\ell$, with the DC and time-modulated biased controlled using voltages V_n. For the 3-coupler circuit, biasing to the central varactor is provided through the resonator.

complex exponentials, as in Eq. (2.18) for $N = 3$. In the Stokes sideband the large transmission dip occurs at $\phi \approx \mp\pi/3$ (minus sign corresponding to minimized forward transmission) corresponding to $\beta\ell = \pi/3$. Figure 3.13a shows simultaneous coupling of both forward and backward waves to the resonance at the lower sideband. This occurs since forward waves couple to the resonator due to the small local maximum of the coupling function, while backward waves couple strongly at the large local maximum. These two local maxima occur for the same modulation phase ϕ due to the waveguide dispersion. The anti-Stokes sideband exhibits similar behavior with one large local coupling maximum at $\phi = \mp\pi/3$ and a smaller local coupling maximum at $\phi \approx 4\pi/3$, corresponding to $\beta\ell = 5\pi/3$. Again, this large difference in $\beta\ell$ between the sidebands can be attributed to non-idealities in the circuit implementation. Figure 3.13**c** shows that on the anti-Stokes sideband the experimental circuit achieves strong coupling for backward waves and essentially zero coupling for forward propagating waves, demonstrating over 7 dB of contrast with $\phi = \pm\pi/3$.

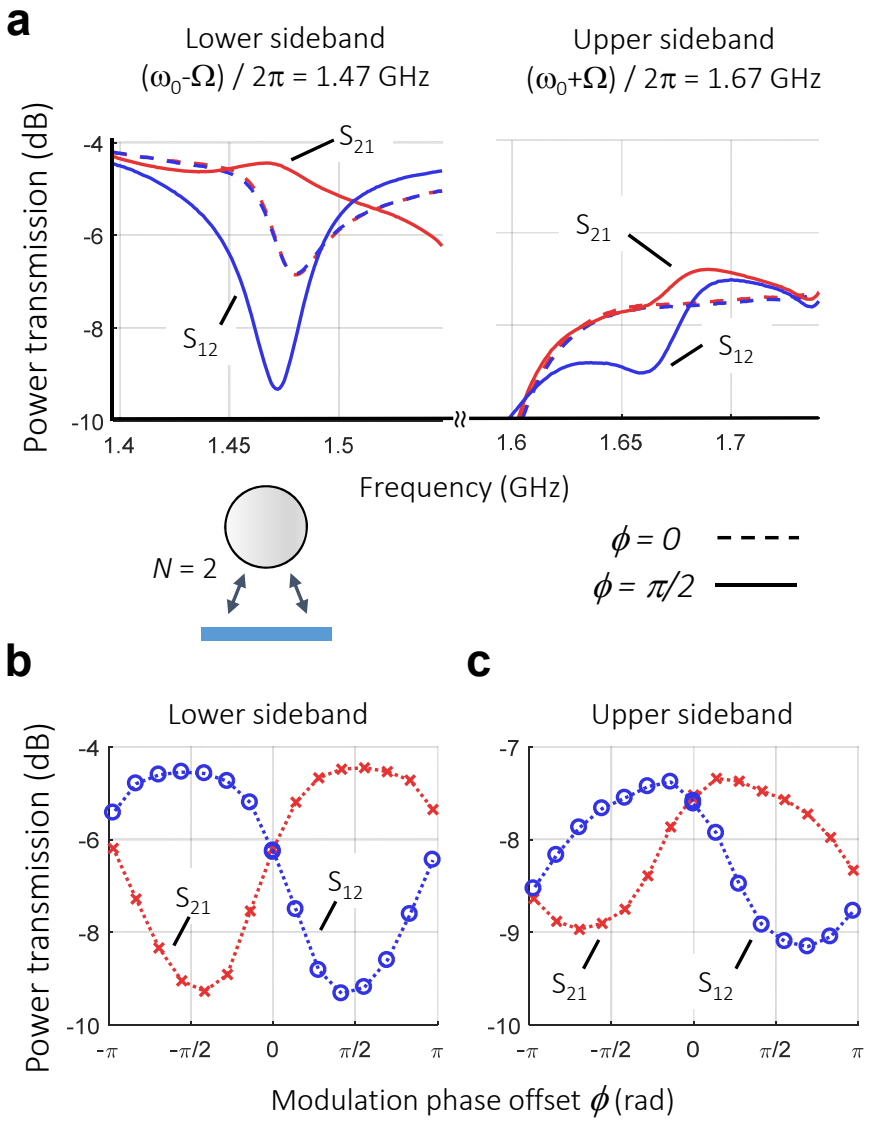

Figure 3.12: (a) Experimentally measured power transmission coefficients for the $N = 2$ circuit are presented at both sidebands using 100 MHz modulation applied to the couplers. Data for forward transmission (S_{21}, red) and backward transmission (S_{12}, blue) are presented for both $\phi = 0$ (dashed lines) and $\phi = \pi/2$ (solid lines). (b,c) Data present the line-center forward (red, x) and backward (blue, o) transmission coefficients at the lower (upper) sideband frequency 1.47 GHz (1.67 GHz) for selected values of ϕ. Nonreciprocal coupling to the resonance is observed while using coupler phase settings of $\phi \neq 0, \pi$ in both upper and lower sidebands of the resonance.

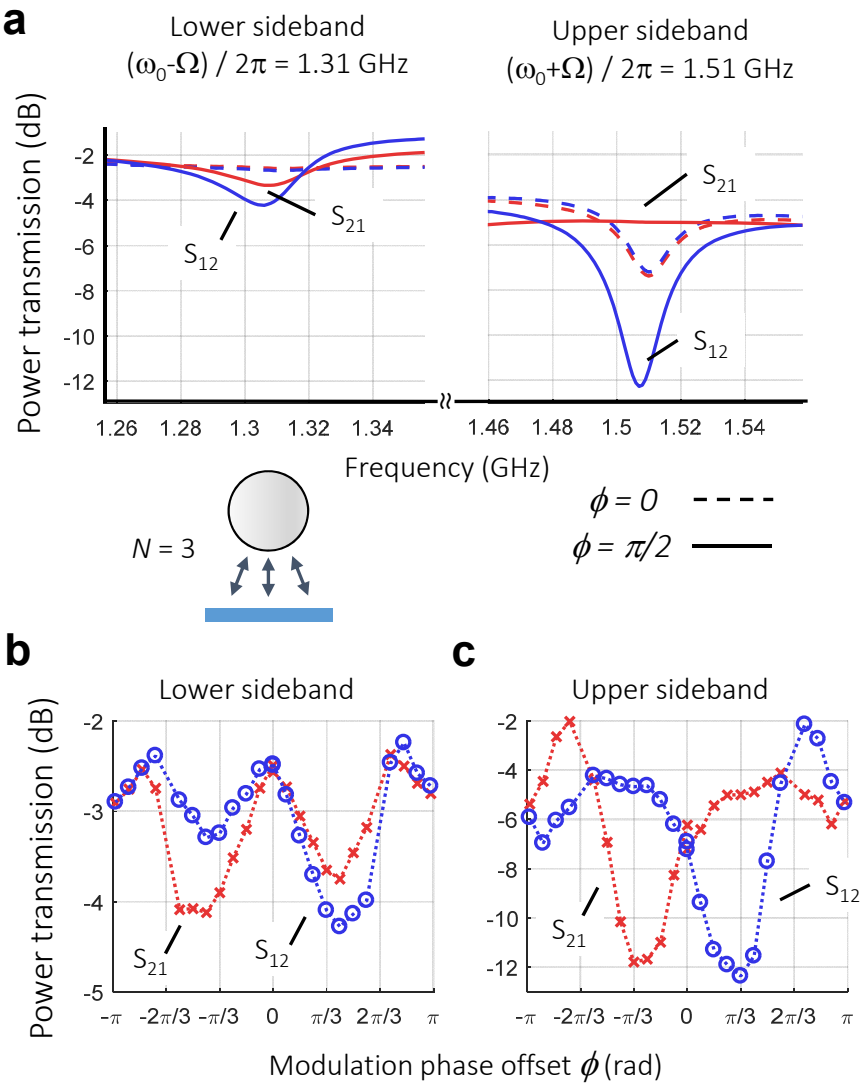

Figure 3.13: (a) Experimentally measured power transmission coefficients for the $N = 3$ circuit are presented at both sidebands using 100 MHz modulation applied to the couplers. Data for forward transmission (S_{21}, red) and backward transmission (S_{12}, blue) are presented for both $\phi = 0$ (dashed lines) and $\phi = \pi/3$ (solid lines). (b,c) Data present the line-center forward (red, x) and backward (blue, o) transmission coefficients at the lower (upper) sideband frequency 1.31 GHz (1.51 GHz) for selected values of ϕ. Nonreciprocal coupling is observed when $\phi \neq 0, \pi$.

Chapter 4

Applications of nonreciprocal coupling

Nonreciprocal devices, such as isolators, gyrators, and circulators, are vital components for advanced signal processing. This chapter discusses how such devices, as well as higher-order nonreciprocal filters, can be constructed using nonreciprocal coupling to resonant modes, as was experimentally demonstrated in the previous chapter. For all of these devices, both the theory of operation and experimental transmission measurements are presented.

4.1 Isolator

An isolator is a two-port nonreciprocal device with high transmission amplitude in one direction and low transmission amplitude in the other. The circuit diagram representation of an isolator is shown in Fig. 4.1. Isolators are commonly used to protect sources (especially in networks of sources), including lasers, RF amplifiers, and high-power signal generators, from potentially harmful back-reflections or interference from other sources, which can cause source instability [58]. The scattering

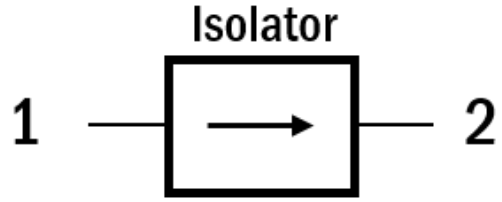

Figure 4.1: Circuit diagram of an isolator.

matrix of an ideal isolator is

$$\hat{S}_{\text{isolator}} = \begin{pmatrix} 0 & 0 \\ 1 & 0 \end{pmatrix} . \tag{4.1}$$

The scattering matrix is not unitary, meaning that an isolator cannot be lossless. In practice isolators are not ideal and always permit some transmission in the backward direction. Typically a magnetic-based isolator will have around 20 dB to 30 dB of isolation contrast (I_{21}^{dB}), where

$$I_{21}^{\text{dB}} = 20\log_{10}|S_{21}| - 20\log_{10}|S_{12}| . \tag{4.2}$$

Isolators based on spatiotemporal modulation have shown isolation ranging from 3 dB [18] to over 50 dB [24]. Note that an ideal isolator has infinite isolation contrast.

Now consider an isolator with high transmission amplitude in the forward direction that operates at the anti-Stokes sideband frequency $\omega_0 + \Omega$. Recalling the transmission equations from Chapter 2,

$$\begin{aligned} S_{21} = e^{-j\beta\ell(N-1)} &- \frac{k_2^0 k_1^0}{j(\omega-\omega_0)+\zeta} - \frac{k_2^- k_1^+}{j(\omega+\Omega-\omega_0)+\zeta} \\ &- \frac{k_2^+ k_1^-}{j(\omega-\Omega-\omega_0)+\zeta} , \end{aligned} \tag{4.3}$$

and

$$\begin{aligned} S_{12} = e^{-j\beta\ell(N-1)} &- \frac{k_1^0 k_2^0}{j(\omega-\omega_0)+\zeta} - \frac{k_1^- k_2^+}{j(\omega+\Omega-\omega_0)+\zeta} \\ &- \frac{k_1^+ k_2^-}{j(\omega-\Omega-\omega_0)+\zeta} , \end{aligned} \tag{4.4}$$

note that the third term (with denominator $j(\omega - \Omega - \omega_0) + \zeta$) corresponds to the anti-Stokes absorption sideband. High transmission is the forward direction and zero transmission is the backward direction occurs at this frequency when $k_1^+ k_2^- = \zeta$ (the critical coupling condition [59]) and $k_2^+ k_1^- = 0$. This case was experimentally

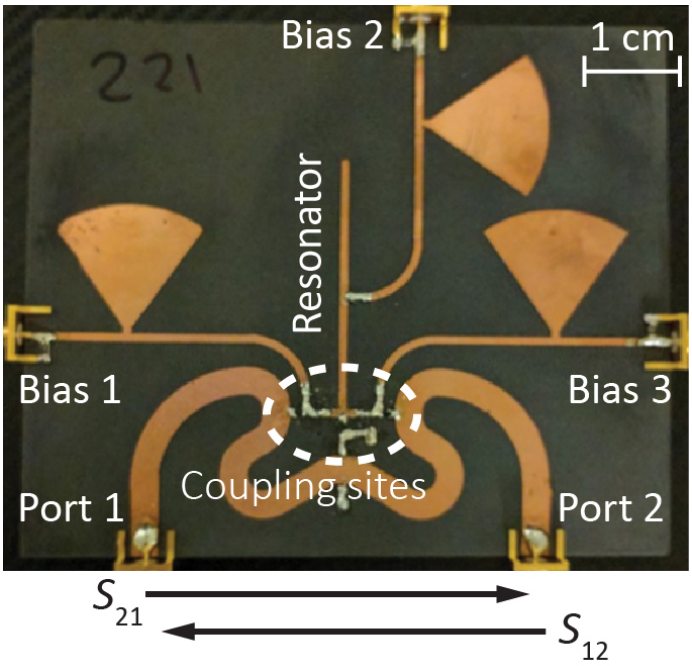

Figure 4.2: Microstrip circuit used to demonstrate nonreciprocal coupling. The circuit consists of a two-port microstrip waveguide and a microstrip stub resonator. Varactor diodes act as voltage-controlled capacitors, which are used to realize modulated coupling rates. The bias ports are used to apply independently controlled voltage biases to the varactor diodes.

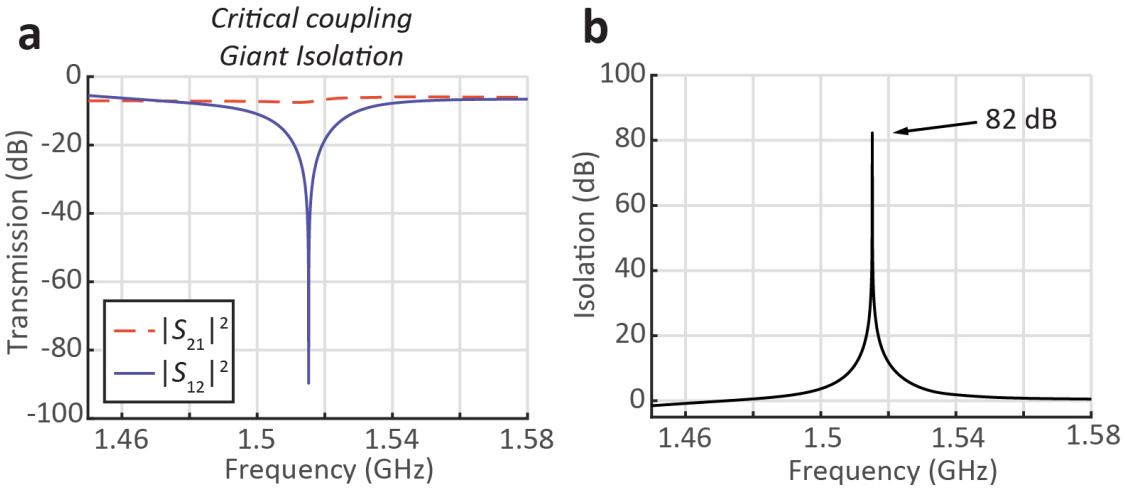

Figure 4.3: Experimentally measured transmission showing complete isolation near the anti-Stokes sideband of a microstrip resonator. **a**, Measured power transmission and phase under the critical coupling condition $C_1^+ C_2^- = \gamma$. There is nearly zero transmission (< -92 dB) through the waveguide in the critically coupled direction. **b**, Measured power isolation when the resonator is critically coupled to one direction of the waveguide through scattering from synthetic phonons. At the resonance frequency measured isolation is 82 dB.

investigated using the circuit shown in Fig. 4.2. The resonance frequency was tuned to $\omega_0/2\pi \approx 1.42$ GHz, and synthetic phonons were again applied with frequency $\Omega/2\pi = 104$ MHz and $q = -k(\omega_0 + \Omega)$. The synthetic phonon amplitude δ_c was increased until the critical coupling condition $k_1^+ k_2^- = \zeta$ was reached. The measured forward (S_{21}) and backward (S_{12}) transmission coefficients for synthetic phonons with this critical amplitude are presented in Fig. 4.3a. A large Lorentzian dip can be observed in the measured backward transmission, which drops to below -89 dB at 1.52 GHz. No resonant absorption is visible in the forward direction. The measured isolation contrast (Fig. 4.3b) exceeds 82 dB with a 10 dB bandwidth of approximately 12 MHz.

4.2 Gyrator

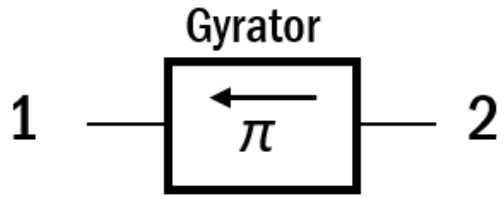

Figure 4.4: Circuit diagram of an isolator.

A gyrator is a two-port nonreciprocal device which has high transmission amplitude in both directions, but a π phase shift between the forward and backward transmission. The gyrator was first proposed by Tellegen as a nonreciprocal circuit-element that could be used to produce any other nonreciprocal circuit [60]. Combinations of gyrators with reciprocal elements can be used to built isolators, circulators, and more complex nonreciprocal networks, making gyrators the fundamental nonreciprocal building block. The circuit diagram representation of a gyrator is shown in Fig. 4.4. The scattering matrix of an ideal gyrator is

$$\hat{S}_{\text{gyrator}} = \begin{pmatrix} 0 & -1 \\ 1 & 0 \end{pmatrix} . \tag{4.5}$$

This matrix is unitary, meaning that an ideal gyrator is lossless. While practical gyrators will always have a small amount of loss, it is important that this loss is equal between the opposite directions of propagation (reciprocal).

Consider a gyrator that operates at the anti-Stoke sideband frequency $\omega_0 + \Omega$. Using the same system as in the previous section, it is evident from Eqs. (4.3) and (4.4) that the gyrator case occurs when the phonon amplitude is increased such that $k_1^+ k_2^- \approx 2\zeta$ (strong over-coupling) while the opposite direction remains uncoupled. Nonreciprocal over-coupling was realized in the same circuit as nonreciprocal critical coupling (Fig. 4.2) by further increasing the synthetic phonon amplitude such that $k_1^+ k_2^- > \zeta$. Figure 4.5a shows the measured transmission with the antici-

pated nonreciprocal π phase shift at the anti-Stokes sideband frequency ≈ 1.52 GHz. Unfortunately, the experimental circuit is unable to realize the required synthetic phonon amplitude to achieve $k_1^+ k_2^- \approx 2\zeta$ due to limitations caused by non-linearity in the varactor diodes. For comparison, the transmission amplitude and phase were also measured in the under-coupled case, where $k_1^+ k_2^- < \zeta$. In this case there is no nonreciprocal π phase shift at the anti-Stokes sideband (Fig. 4.5b).

4.3 Circulator

A circulator is a nonreciprocal device which "circulates" inputs between three or more ports. The circuit diagram representation of a circulator is shown in Fig. 4.6. Circulators are used for many signal processing applications, including in sensitive quantum measurements [61] and to enable full duplex communication [62]. Circulators can also be used to turn one-port amplifiers into two-port amplifiers, and in combining multiple signals without interfering with the signal sources [58]. The scattering matrix of a three port circulator is

$$\hat{S}_{\text{circ},3} = \begin{pmatrix} 0 & 0 & 1 \\ 1 & 0 & 0 \\ 0 & 1 & 0 \end{pmatrix} , \tag{4.6}$$

and the scattering matrix of a four port circulator is

$$\hat{S}_{\text{circ},4} = \begin{pmatrix} 0 & 0 & 0 & 1 \\ 1 & 0 & 0 & 0 \\ 0 & 1 & 0 & 0 \\ 0 & 0 & 1 & 0 \end{pmatrix} . \tag{4.7}$$

These matrices are unitary, meaning that ideal circulators are lossless. The circulator scattering matrix clearly shows the "circulating" behavior: a signal travels from ports $1 \to 2$, $2 \to 3$, $3 \to 4$, etc.

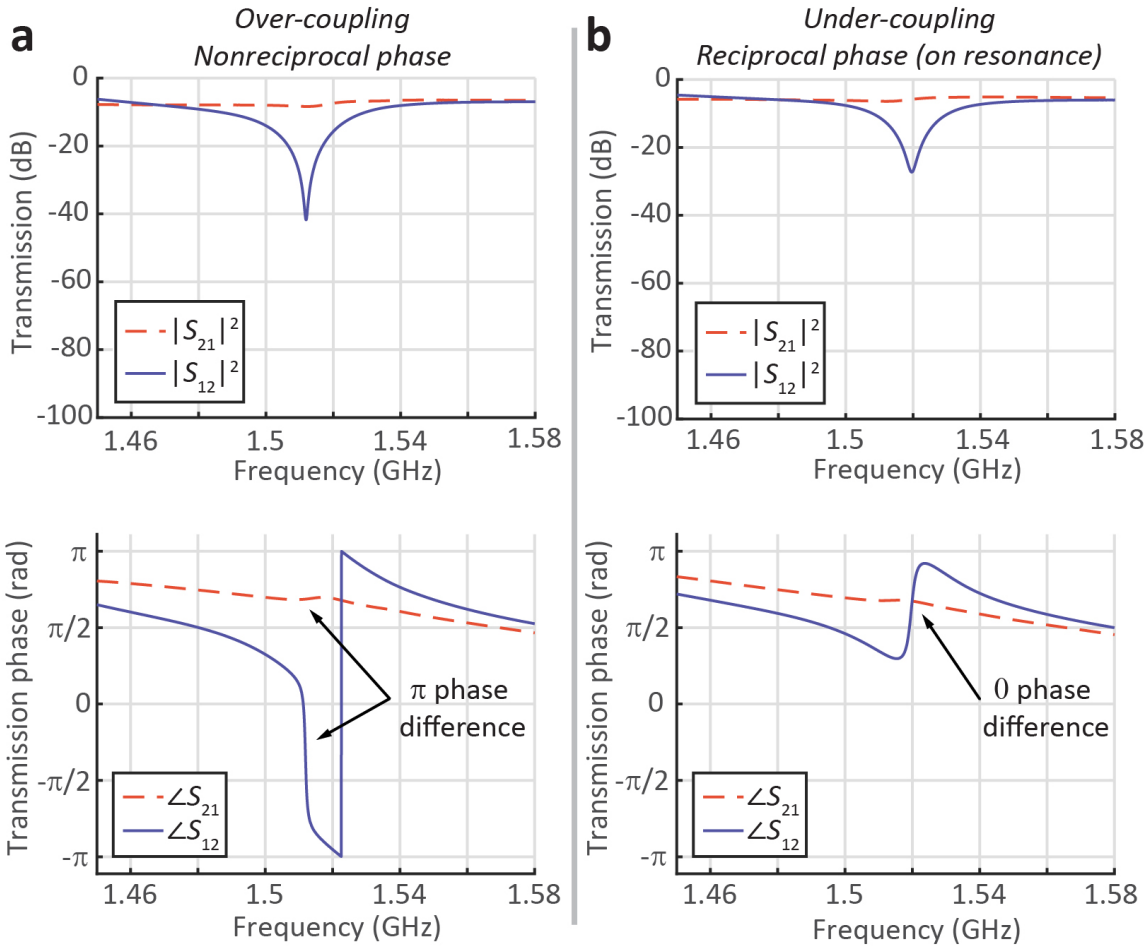

Figure 4.5: Experimentally measured transmission showing nonreciprocal phase shifts near the anti-Stokes sideband of a microstrip resonator. **a**, Measured power transmission amplitude and phase for above-critical synthetic phonon amplitude. The resonator is over-coupled and there is a π nonreciprocal phase shift at the anti-Stokes sideband frequency. **b**, Measured power transmission amplitude and phase for below-critical synthetic phonon amplitude. The resonator is under-coupled and there is no phase shift at the anti-Stokes sideband frequency.

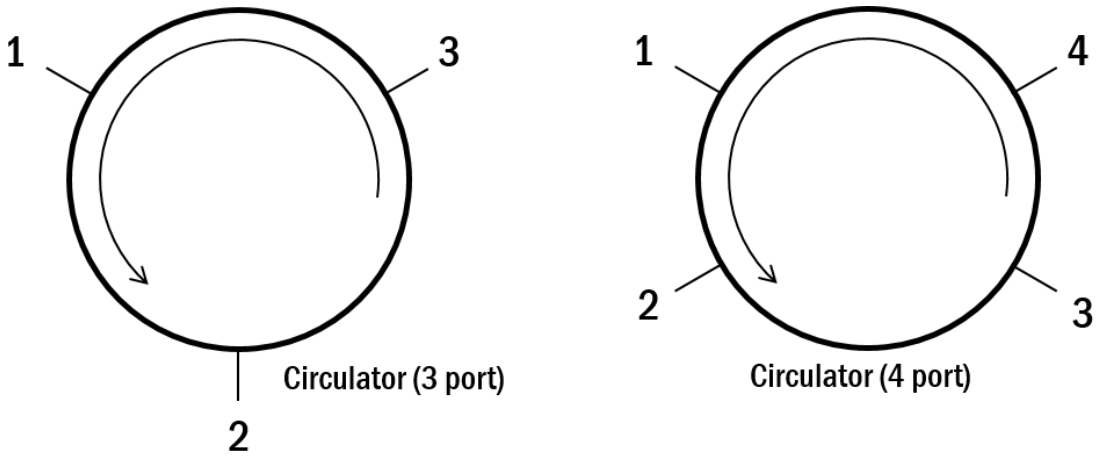

Figure 4.6: Circuit diagrams of a three (left) and four (right) port circulator. The arrows indicate the circulation direction.

Using two waveguides and a single resonator, it is possible to realize a four-port circulator through synthetic phonon enabled nonreciprocal coupling. Since there are four ports, the additional coupling constants k_3 and k_4 are introduced to couple the resonator to ports 2 and 3 respectively, as illustrated in Fig. 4.7a. These additional coupling constants can be expressed in the same way as the coupling constants on the original waveguide,

$$\begin{aligned} k_1 = k_3 &= \sum_{n=1}^{N} c_n e^{-j\beta\ell(n-1)} \ , \\ k_2 = k_4 &= \sum_{n=1}^{N} c_n e^{j\beta\ell(n-1)} \ . \end{aligned} \tag{4.8}$$

Using the same synthetic phonon definition on both sets of coupling constants,

$$c_n = c_0 + \delta_c \cos(\Omega t - q\ell(n-1)) \ , \tag{4.9}$$

we can again separate the coupling into components with no frequency shift, a posi-

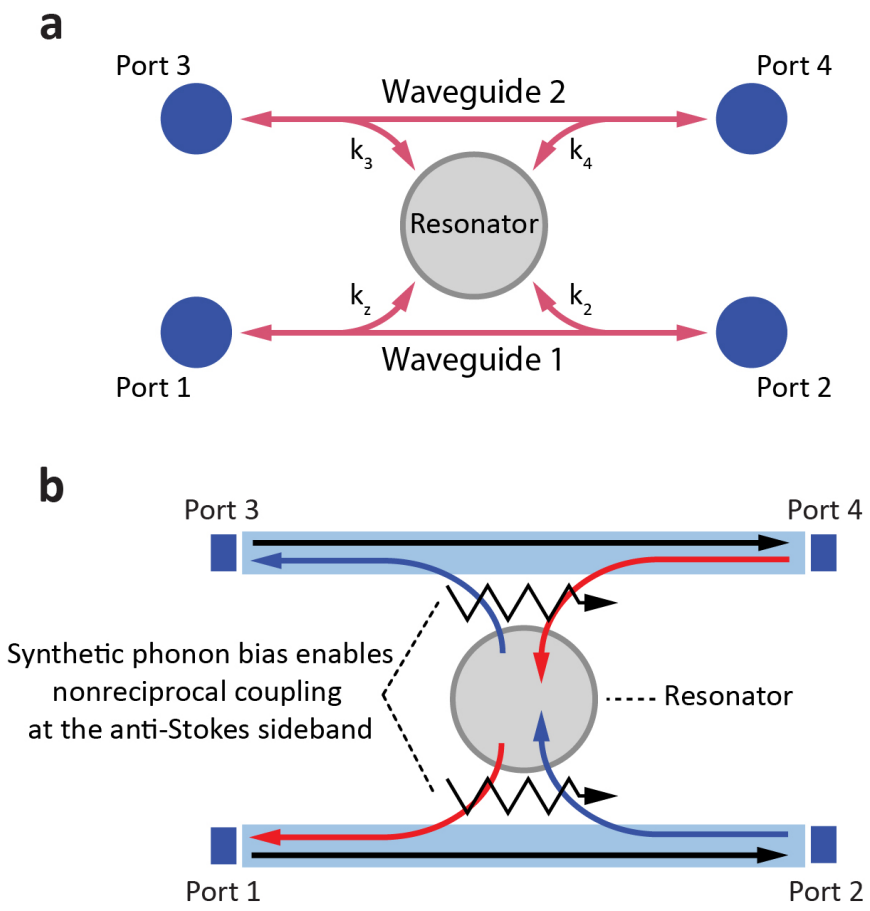

Figure 4.7: **a**, Diagram of the coupling constants k_{1-4} which connect the ports to the resonator. **b**, Schematic of the proposed circulator design. Arrows correspond to the high transmission pathways: S_{21} and S_{34} (black), S_{23} (blue), and S_{41} (red).

tive frequency shift, and a negative frequency shift as

$$k_1 = k_3 = \overbrace{c_0 \sum_{n=1}^{N} e^{-j\beta\ell(n-1)}}^{k_1^0,\ k_3^0} + \overbrace{\frac{c_M}{2} e^{j\Omega t} \sum_{n=1}^{N} e^{-j(\beta+q)\ell(n-1)}}^{k_1^+,\ k_3^+} + \overbrace{\frac{c_M}{2} e^{j\Omega t} \sum_{n=1}^{N} e^{-j(\beta-q)\ell(n-1)}}^{k_1^-,\ k_3^-}, \tag{4.10}$$

and

$$k_2 = k_4 = \overbrace{c_0 \sum_{n=1}^{N} e^{j\beta\ell(n-1)}}^{k_2^0,\ k_4^0} + \overbrace{\frac{c_M}{2} e^{j\Omega t} \sum_{n=1}^{N} e^{j(\beta-q)\ell(n-1)}}^{k_2^+,\ k_4^+} + \overbrace{\frac{c_M}{2} e^{-j\Omega t} \sum_{n=1}^{N} e^{j(\beta+q)\ell(n-1)}}^{k_2^-,\ k_4^-}. \tag{4.11}$$

For the four port circulator, the transmission coefficients between ports 1 and 2 (and 3 and 4) are the same as in the single waveguide case, and transmission through the resonator takes the form

$$S_{31} = -\frac{k_3^0 k_1^0}{j(\omega-\omega_0)+\zeta} - \frac{k_3^- k_1^+}{j(\omega+\Omega-\omega_0)+\zeta} - \frac{k_3^+ k_1^-}{j(\omega-\Omega-\omega_0)+\zeta}, \tag{4.12}$$

since there is no direct path connecting the ports. The new scattering matrix parameters can be calculated using the same derivation as presented in Chapter 2. The principle of operation of the circulator can be described in terms of indirect transitions, as shown in Fig. 4.8.

As in the previous sections, consider a device that functions at the anti-Stokes sideband frequency. The circulation behavior is illustrated in Fig. 4.7b. If the resonator is critically coupled to the backward direction of each waveguide such that

$k_1^+ k_2^- = k_3^+ k_4^- = \zeta$ and $k_1^- k_2^+ = k_3^- k_4^+ = 0$, the scattering matrix is

$$|\hat{S}(\omega_0 + \Omega)|^2 = \begin{pmatrix} 0 & 0 & 0 & 1 \\ 1 & 0 & 0 & 0 \\ 0 & 1 & 0 & 0 \\ 0 & 0 & 1 & 0 \end{pmatrix} , \tag{4.13}$$

which is the definition of an ideal four-port circulator. Note that due to the additional coupling terms between the resonator and second waveguide, decay of the resonant mode to the ports increases proportionally as

$$2\gamma = \langle k_1 k_1^* + k_2 k_2^* + k_3 k_3^* + k_4 k_4^* \rangle . \tag{4.14}$$

From this equation we can see that this ideal device, which is critically coupled in both directions

$$\zeta = \frac{k_1^+ k_2^-}{2} + \frac{k_3^+ k_4^-}{2}, \tag{4.15}$$

can only be realized with a lossless resonator ($\kappa = 0$) since by definition

$$\zeta \geq \frac{k_1^+ k_2^-}{2} + \frac{k_3^+ k_4^-}{2} + \kappa . \tag{4.16}$$

However an ideal circulator can be approximated by making κ small compared to the coupling rates, and ensuring that minimal coupling occurs to the backward direction.

A four-port circulator was implemented using a similar circuit as the isolator and gyrator, but with an additional waveguide having three coupling sites (Fig. 4.9a). Synthetic phonons were applied to each trio of coupling sites with the same bias voltage to ensure symmetric coupling $k_1 = k_3$ and $k_2 = k_4$. The measured transmission (Fig. 4.9b) shows clear circulation behavior, with high transmission from ports $1 \rightarrow 2$, $2 \rightarrow 3$, $3 \rightarrow 4$ (not shown), and $4 \rightarrow 1$, and low transmission in the opposite direction.

Since the intrinsic loss rate in the resonator (κ) is not negligible in this experiment, the critical coupling condition for near-ideal circulation cannot be achieved. The

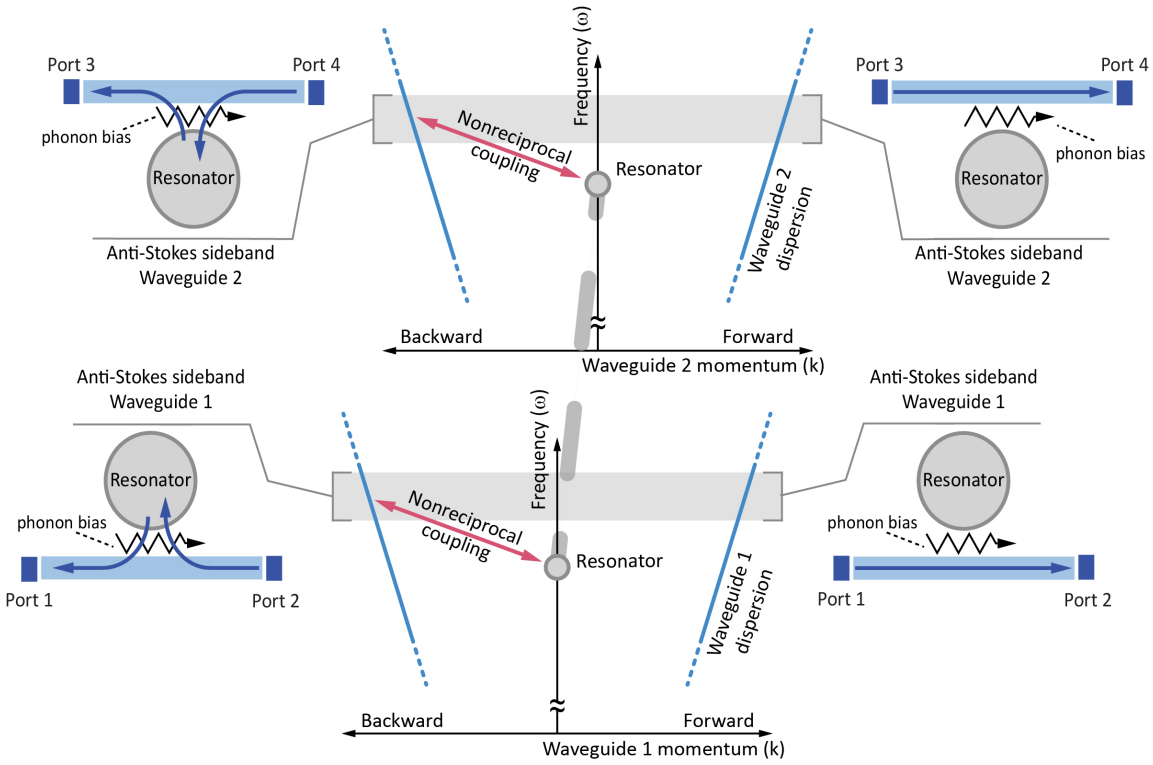

Figure 4.8: Frequency-momentum diagram illustrating nonreciprocal coupling (pink arrows) at the anti-Stokes sideband, as used in the circulator design in (b). Due to the phase matching requirement, the synthetic phonon bias only couples the backward mode (port $2 \rightarrow 1$ or $4 \rightarrow 3$) in each waveguide to the resonator.

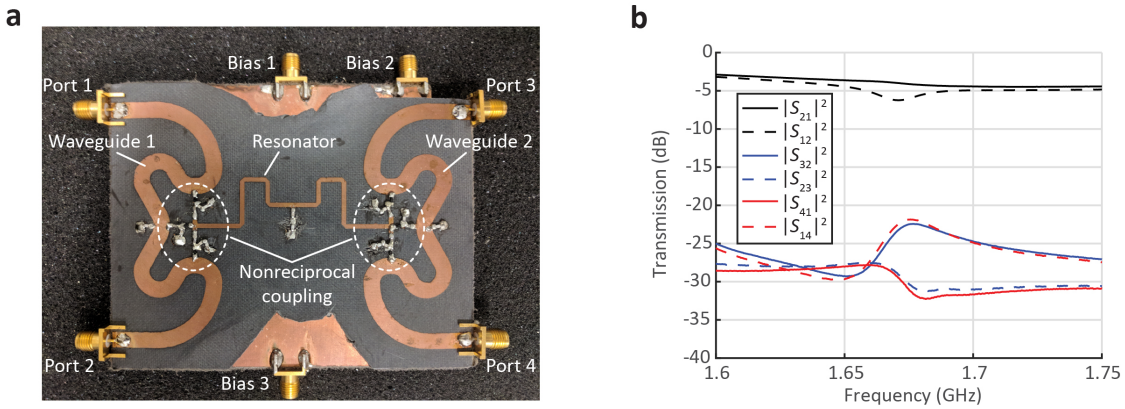

Figure 4.9: **a**, Photograph of the circuit implementing the circulator design in Fig. 4.9(b) with three coupling sites between each waveguide and the resonator. **b**, Measured power transmission for the circuit in (a), under a synthetic phonon bias which maximizes $k_1^+ k_2^-$ and $k_3^+ k_4^-$. Colors correspond to the arrow colors in Fig. 4.9(b). Unshown transmission coefficients S_{43} and S_{34} are equal to S_{21} and S_{12} respectively, due to mirror symmetry. All other unshown transmission coefficients are reciprocal.

presence of coupling at the Stokes sideband and the original resonance frequency, although small, also increases the decay rate as described by Eq. (4.14). Due to these limitations, the circulator exhibits low contrast between S_{21} and S_{12}, and the measured transmission between ports on opposite waveguides is highly lossy. These challenges could be addressed with a higher Q-factor resonator or by increasing the nonreciprocal coupling rate. Additionally, by increasing the number of coupling sites (N) and thereby making the phase matching condition more strict, coupling at the Stokes sideband and original resonance frequency can be decreased. The increased number of coupling sites would also increase the nonreciprocal coupling rate, which is proportional to N^2. Despite the current challenges, this experiment provides clear evidence that circulation using synthetic phonon enabled coupling is possible.

4.4 Higher-order nonreciprocal filters

Higher-order filters are necessary for many signal processing applications [41, 42]. Such filters can realize frequency responses that are not possible with first-order filters, such as maximally flat responses [63] or multiple sharp features. However, frequency-selective nonreciprocal filters (frequency selective isolators) have so far been limited to first-order Lorentizian responses [18, 19, 20, 22, 23, 24, 62]. Higher-order nonreciprocal filters have potential for use in any signal processing application which requires a specific frequency response that differs depending on the direction of propagation. Synthetic phonon-enabled coupling is a technique uniquely suited to address this challenge because it can permit unidirectional access to arbitrary band-limited load impedances (Fig. 4.10a), producing arbitrary nonreciprocal responses. Additionally, different frequency responses could be simultaneously achieved in opposite directions by coupling each direction to an appropriate resonator network [43].

Implementing this idea, this section provides experimental demonstrations of non-Lorentzian nonreciprocal transfer functions. All experiments were done using the circuit shown in Fig. 4.10b, which is a modified version of that in Fig. 3.9. In the modified circuit, two additional microstrip stub resonators with tunable resonance frequencies are coupled to the original stub resonator used in previous experiments (Fig. 4.10b), providing six additional degrees of freedom: the additional resonance frequencies $\omega_1,\ \omega_2$, inter-resonator coupling rates $\kappa_1,\ \kappa_2$, and linewidths $\zeta_1,\ \zeta_2$.

A maximally flat nonreciprocal filter with constant isolation over an appreciable bandwidth is arguably one of the most important functionalities that cannot be implemented using a single resonant response. Such a flat response can be approximated in the three resonator network using $\zeta_1 = \zeta_2 = \zeta$, $\kappa_1 = \kappa_2 = \frac{9}{14}\zeta$, $\omega_1 = \omega_0 + \frac{3}{7}\zeta$, and $\omega_2 = \omega_0 - \frac{3}{7}\zeta$, where the loss rate ζ and resonance frequency ω_0 are associated with the original resonator. Both the resonance frequencies ($\omega_1,\ \omega_2$) and coupling rates (κ_1, κ_2) of the additional resonators in the circuit (Fig. 4.10b) were tuned near these values until the desired transfer function was achieved. Since the resonators are fabricated on the same substrate and conductor, their linewidths are intrinsically

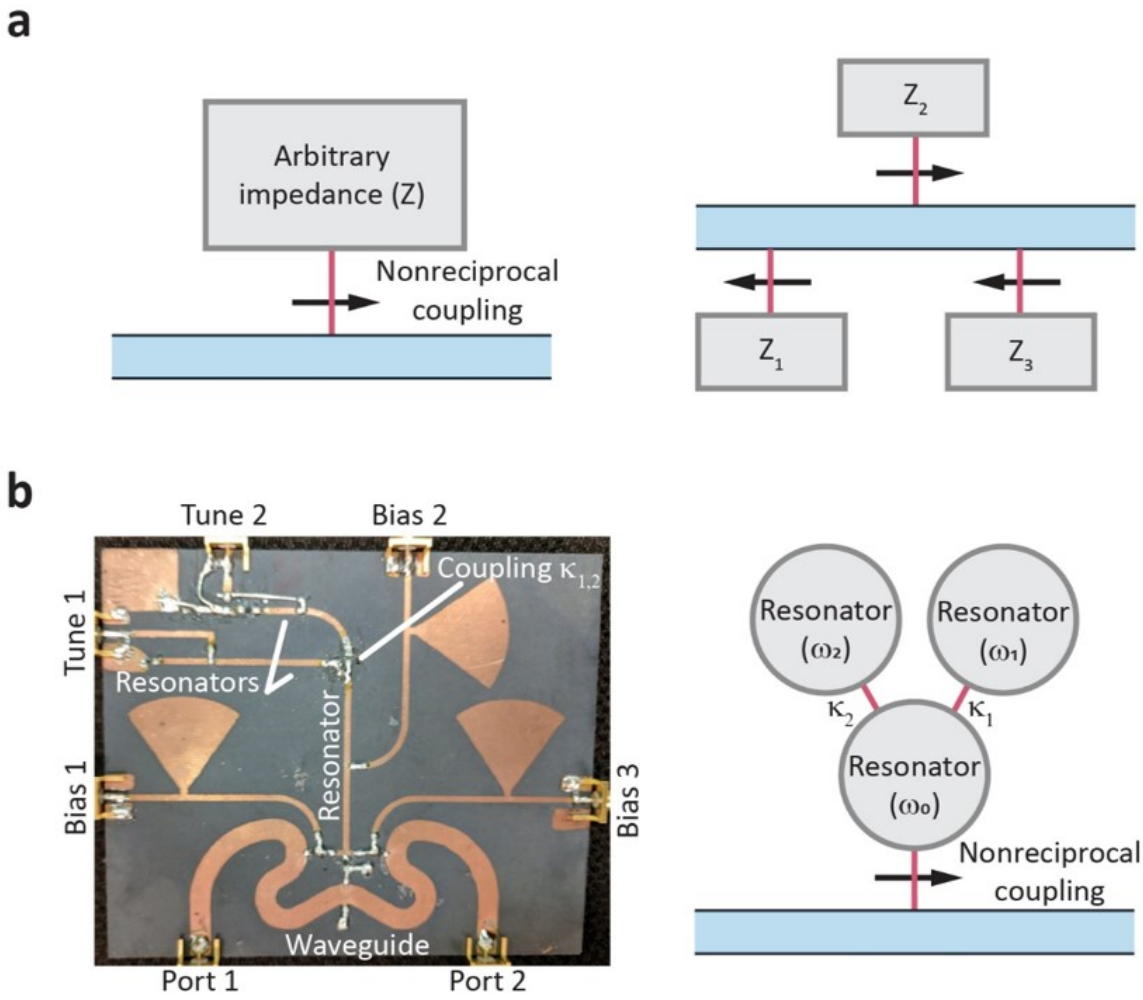

Figure 4.10: (a) Nonreciprocal coupling can be engaged to an arbitrary band-limited impedance network. Several of these impedance networks can be simultaneously coupled in either direction to create customizable responses. (b) Photograph (left) and schematic (right) of the circuit used to demonstrate customizable nonreciprocal transfer functions.

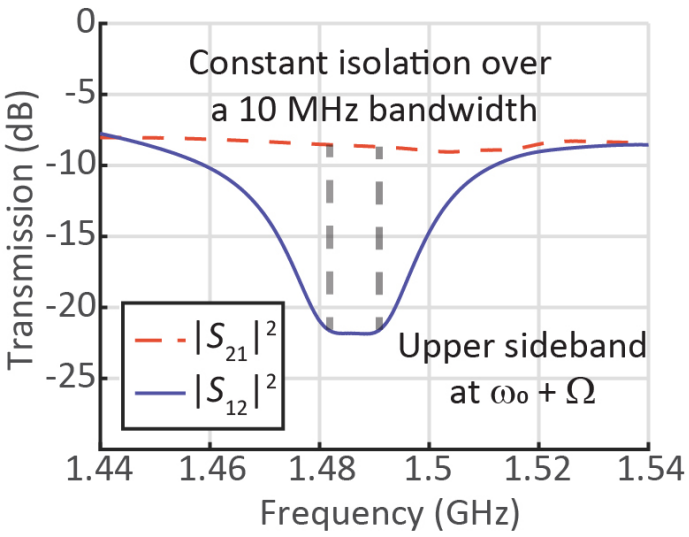

Figure 4.11: Measured power transmission showing a flat band over which a constant isolation is obtained.

equal. The experimentally measured transmission through the waveguide (Fig. 4.11) exhibits nearly constant isolation of 14 dB over a 10 MHz bandwidth.

Figure 4.12 shows four additional examples of arbitrary nonreciprocal transfer functions obtained by varying the inter-resonator coupling strength and frequency separation of the three resonators. In these experiments, the forward transmission (S_{21}) is consistently flat even though the reverse transmission (S_{12}) varies, clearly demonstrating that propagation in the uncoupled direction is largely unaffected by changes to the impedance network.

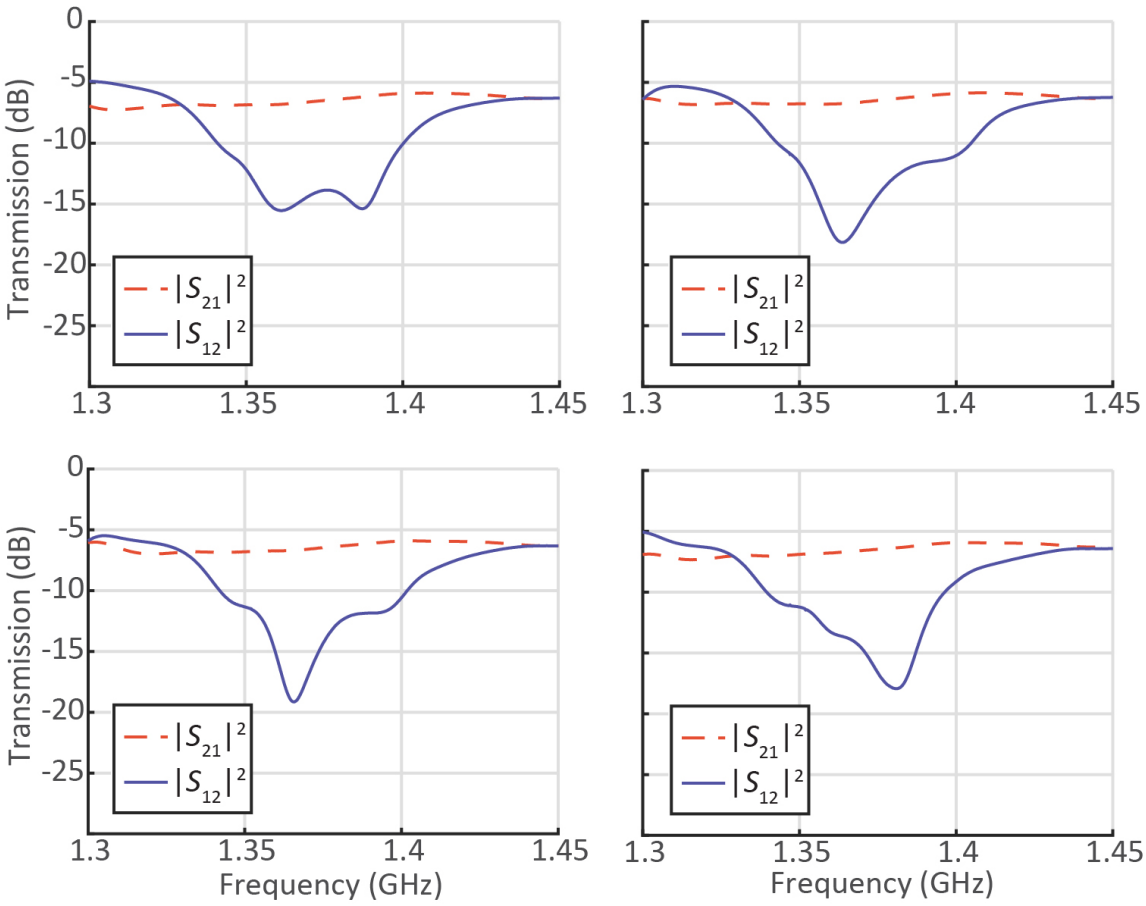

Figure 4.12: Experimental demonstration of four distinct nonreciprocal transfer functions obtained by tuning the resonator network.

Chapter 5

Conclusions

This work has proposed a method for generating indirect photonic transitions between a waveguide and resonator to produce a variety of nonreciprocal devices. Beginning from temporal coupled mode theory, it was shown that such indirect transitions can be induced by modulating the coupling constants of multiple spatially separated coupling sites between a waveguide and resonator. This modulation was termed a "synthetic phonon" in an analogy to phonons in crystals, which modulate the atomic positions in much the same way that the coupling constants are modulated. Phonons in crystals can induce indirect electronic transitions, while synthetic phonons can induce indirect photonic transitions. The indirect photonic transitions between a waveguide and resonator lead to a phenomenon termed "nonreciprocal coupling", where different directions of the waveguide couple to the resonator differently.

Nonreciprocal coupling was explored experimentally using microwave frequency circuits. Microstrip waveguides were used to implement direct connections between ports, while microstrip stub and ring resonators approximated the idealized resonances of coupled-mode theory. Capacitance was found to be linearly proportional to the coupling constants in coupled-mode theory, so the time-varying coupling constants between the waveguides and resonator were implemented using varactor diodes, which change their capacitance in response to an applied voltage. Using circuits constructed in this manner, nonreciprocal coupling was experimentally demonstrated and the theory's prediction that the coupling rate would depend on the momentum of the applied synthetic phonons was verified. Several nonreciprocal devices, the isolator, gyrator, and circulator, were demonstrated using nonreciprocal

coupling in microstrip circuits. Additionally a new device, a higher-order nonreciprocal filter, was demonstrated using nonreciprocal coupling to a network of resonators. Nonreciprocal coupling between waveguides and resonator is clearly a powerful tool, since it can be used to realize fundamental nonreciprocal devices as well as more complex ones.

Although initial experiments have shown that nonreciprocal coupling could be used to produce a variety of nonreciprocal devices, there is still much work to be done. Presently, the experimental circuits are unable to observe lossless nonreciprocal transmission due to several non-ideal factors in the design. Specifically, in circuit implementation of a waveguide and ring resonator coupled with discrete capacitors there are several effects that are not accounted for in the temporal coupled-mode theory the most important of which are reflections from the capacitive couplers that can significantly distort the resonance shape and the slightly non-linear response of the varactor diodes. Due to this effect we observe scattering from the modulated couplers even far from the resonance, which effectively creates extra loss in the system. This behavior could be overcome in circuit implementations by lowering the intrinsic losses in the resonator and using a smaller capacitance for coupling. These modifications will decrease the distortion of the resonance shape as well as the non-linearity introduced by the varactor diodes.

Although our experiments take place in microstrip circuits, the nonreciprocal behavior of our system is captured by coupled-mode theory and thus the underlying method can be extended to a wide variety of physical systems. Nonreciprocal coupling could be implemented in optical, acoustic, and mechanical systems, providing a platform for customizable nonreciprocity in each of these domains. Additionally, the concept of nonreciprocal coupling can be applied broadly to a number of band-limited devices besides resonators, including antennas, amplifiers, oscillators, and sensors, allowing the creation of highly customizable integrated devices.

References

[1] C. W. Peterson, S. Kim, J. T. Bernhard, and G. Bahl, "Reconfigurable arbitrary nonreciprocal transfer functions through nonreciprocal coupling," *arXiv:1702.06476*, 2017.

[2] J. W. Strutt, "Some general theorems relating to vibrations," *Proceedings of the London Mathematical Society*, vol. 4, pp. 357–368, 1873.

[3] J.-M. Jin, *Theory and Computation of Electromagnetic Fields*. Hoboken, New Jersey: John Wiley and Sons, 2010.

[4] J. R. Carson, "A generalization of the reciprocal theorem," *The Bell System Technical Journal*, vol. 3, pp. 393–399, 1924.

[5] D. M. Pozar, *Microwave Engineering*. Hoboken, New Jersey: Wiley, 2004.

[6] C. L. Hogan, "The ferromagnetic Faraday effect at microwave frequencies and its applications — The microwave gyrator," *The Bell System Technical Journal*, vol. 31, pp. 1–31, Jan 1952.

[7] H. B. G. Casimir, "Reciprocity theorems and irreversible processes," *Proceedings of the IEEE*, vol. 51, no. 11, pp. 1570–1573, Nov 1963.

[8] L. Fan, J. Wang, L. T. Varghese, H. Shen, B. Niu, Y. Xuan, A. M. Weiner, and M. Qi, "An all-silicon passive optical diode," *Science*, vol. 335, pp. 447–450, 2012.

[9] B. Peng, S. K. Ozdemir, F. Lei, F. Monifi, M. Gianfreda, G. L. Long, S. Fan, F. Nori, C. M. Bender, and L. Yang, "Parity-time-symmetric whispering-gallery microcavities," *Nature Physics*, vol. 10, pp. 394–398, 2014.

[10] Y. Shi, Z. Yu, and S. Fan, "Limitations of nonlinear optical isolators due to dynamic reciprocity," *Nature Photonics*, vol. 9, pp. 388–392, 2015.

[11] D. L. Sounas, J. Soric, and A. Alú, "Broadband passive isolators based on coupled nonlinear resonances," *Nature Electronics*, vol. 1, pp. 113–119, 2018.

[12] I. K. Hwang, S. H. Yun, and B. Y. Kim, "All-fiber-optic nonreciprocal modulator," *Optics Letters*, vol. 22, pp. 507–509, 1997.

[13] Z. Yu and S. Fan, "Complete optical isolation created by indirect interband photonic transisions," *Nature Photonics*, vol. 3, pp. 91–94, 2008.

[14] A. Kamal, J. Clarke, and M. H. Devoret, "Noiseless non-reciprocity in a parametric active device," *Nature Physics*, vol. 7, pp. 311–315, 2011.

[15] M. S. Kang, A. Butsch, and P. S. J. Russell, "Reconfigurable light-driven optoacoustic isolators in photonic crystal fibre," *Nature Photonics*, vol. 5, pp. 549–553, 2011.

[16] M. Hafezi and P. Rabl, "Optomechanically induced non-reciprocity in microring resonators," *Optics Express*, vol. 20, pp. 7672–7684, 2012.

[17] C. G. Poulton, R. Pant, A. Byrnes, S. Fan, M. J. Steel, and B. J. Eggleton, "Design for broadband on-chip isolator using stimulated Brillouin scattering in dispersion-engineered chalcogendide waveguides," *Optics Express*, vol. 20, pp. 21 235–21 246, 2012.

[18] H. Lira, Z. Yu, S. Fan, and M. Lipson, "Electrically driven nonreciprocity induced by interband photonic transition on a silicon chip," *Physical Review Letters*, vol. 109, p. 033901, 2012.

[19] R. Fleury, D. L. Sounas, C. F. Sieck, M. R. Haberman, and A. Alú, "Sound isolation and giant linear nonreciprocity in a compact acoustic circulator," *Science*, vol. 343, pp. 516–519, 2014.

[20] N. A. Estep, D. L. Sounas, J. Soric, and A. Alú, "Magnetic-free non-reciprocity and isolation based on parametrically modulated coupled-resonator loops," *Nature Physics*, vol. 10, pp. 923–927, 2014.

[21] S. Qin, Q. Xu, and Y. E. Wang, "Nonreciprocal components based on distributed modulated capacitors," *IEEE Transactions on Microwave Theory and Techniques*, vol. 62, no. 10, pp. 2260–2272, 2014.

[22] J. Kim, M. C. Kuzyk, K. Han, H. Wang, and G. Bahl, "Non-reciprocal Brillouin scattering induced transparency," *Nature Physics*, vol. 11, pp. 275–280, 2015.

[23] C.-H. Dong, Z. Shen, C.-L. Zou, Y.-L. Zhang, W. Fu, and G.-C. Guo, "Brillouin-scattering-induced transparency and non-reciprocal light storage," *Nature Communications*, vol. 6, p. 6193, 2015.

[24] N. A. Estep, D. L. Sounas, and A. Alú, "Magnetless microwave circulators based on spatiotemporally modulated rings of coupled resonators," *IEEE Transactions on Microwave Theory and Techniques*, vol. 64, pp. 502–518, 2016.

[25] Z. Shen, Y.-L. Zhang, Y. Chen, C.-L. Zou, Y.-F. Xiao, X.-B. Zou, F.-W. Sun, G.-C. Guo, and C.-H. Dong, "Experimental realization of optomechanically induced non-reciprocity," *Nature Photonics*, vol. 10, pp. 657–661, 2016.

[26] J. Kim, S. Kim, and G. Bahl, "Complete linear optical isolation at the microscale with ultralow loss," *Sci. Rep.*, vol. 7, p. 1647, 2017.

[27] S. Kim, X. Xu, J. M. Taylor, and G. Bahl, "Dynamically induced robust phonon transport and chiral cooling in an optomechanical system," *Nature Communications*, vol. 8, p. 205, 2017.

[28] Y. Shi, S. Han, and S. Fan, "Optical circulation and isolation based on indirect photonic transitions of guided resonance modes," *ACS Photonics*, vol. 4, no. 7, pp. 1639–1645, 2017.

[29] K. Hess, *Advanced Theory of Semiconductor Devices*. Hoboken, New Jersey: John Wiley and Sons, 2000.

[30] J. N. Winn, S. Fan, J. D. Joannopoulos, and E. P. Ippen, "Interband transitions in photonic crystals," *Physical Review B*, vol. 59, no. 3, pp. 1551–1554, 1999.

[31] L. Kuhn, P. F. Heidrich, and E. G. Lean, "Optical guided wave mode conversion by an acoustic surface wave," *Appl. Phys. Lett.*, vol. 19, pp. 428–430, 1971.

[32] I. K. Hwang, S. H. Yun, and B. Y. Kim, "All-fiber-optic nonreciprocal modulator," *Optics Lett.*, vol. 22, no. 8, pp. 507–509, 1997.

[33] J. D. Joannopoulos, P. R. Villeneuve, and S. Fan, "Photonic crystals: putting a new twist on light," *Nature*, vol. 386, pp. 143–149, 1997.

[34] R. W. Boyd, *Nonlinear Optics*. Cambridge, Massachusettes: Academic Press, 2003.

[35] P. Dong, S. F. Preble, J. T. Robinson, S. Manipatruni, and M. Lipson, "Inducing photonic transitions between discrete modes in a silicon optical microcavity," *Phys. Rev. Lett.*, vol. 100, p. 033904, 2008.

[36] H. Dötsch, N. Bahlmann, O. Zhuromskyy, M. Hammer, L. Wilkens, R. Gerhardt, P. Hertel, and A. F. Popkov, "Applications of magneto-optical waveguides in integrated optics: review," *J. Opt. Soc. Am. B*, vol. 22, pp. 240–253, 2005.

[37] F. Arecchi and R. Bonifacio, "Theory of optical maser amplifiers," *IEEE Journal of Quantum Electronics*, vol. 1, no. 4, pp. 169–178, 1965.

[38] H. Haus, *Waves and Fields in Optoelectronics*. Englewood Cliffs, New Jersey: Prentice-Hall, 1984.

[39] D. B. Sohn, S. Kim, and G. Bahl, "Time-reversal symmetry breaking with acoustic pumping of nanophotonic circuits," *Nature Photonics*, vol. 12, pp. 91–97, 2018.

[40] A. Ishikawa and K. Tsuruta, "Design of non-reciprocal acoustic waveguides by indirect interband transitions," *Japanese Journal of Applied Physics*, vol. 56, no. 751, p. 07JB01, 2017.

[41] B. E. Little, S. T. Chu, H. A. Haus, J. Foresi, and J.-P. Laine, "Microring resonator channel dropping filters," *Journal of Lightwave Technology*, vol. 15, no. 6, pp. 998–1005, 1997.

[42] J. V. Hryniewicz, P. P. Absil, B. E. Little, R. A. Wilson, and P.-T. Ho, "Higher order filter response in coupled microring resonators," *IEEE Photonics Tech. Lett.*, vol. 12, no. 3, pp. 320–322, 2000.

[43] R. Orta, P. Savi, R. Tascone, and D. Trinchero, "Synthesis of multiple-ring-resonator filters for optical systems," *IEEE Photonics Tech. Lett.*, vol. 7, no. 12, pp. 1447–1449, 1995.

[44] K.-J. Boller, A. Imamoglu, and S. E. Harris, "Observation of electromagnetically induced transparency," *Phys. Rev. Lett.*, vol. 66, no. 20, pp. 2593–2596, 1991.

[45] E. Arimondo, "Coherent population trapping in laser spectroscopy," in *Progress in Optics*. Elsevier, Amsterdam, 1996, vol. 35, pp. 257–354, jILA Pub. 5423.

[46] C. W. Hsu, B. Zhen, A. D. Stone, J. D. Joannopoulos, and M. Soljačić, "Bound states in the continuum," *Nature Reviews Materials*, vol. 1, p. 16048, 2016.

[47] F. Monticone and A. Alù, "Embedded photonic eigenvalues in 3D nanostructures," *Phys. Rev. Lett.*, vol. 112, p. 213903, 2014.

[48] C. Dong, V. Fiore, M. C. Kuzyk, and H. Wang, "Optomechanical dark mode," *Science*, vol. 338, pp. 1609–1613, 2012.

[49] Q.-H. Guo, M. Kang, T.-F. Li, H.-X. Cui, and J. Chen, "Slow light from sharp dispersion by exciting dark photonic angular momentum states," *Optics Letters*, vol. 38, no. 3, pp. 250–252, 2013.

[50] M. Yang, T.-F. Li, Q.-W. Sheng, T.-J. Guo, Q.-H. Guo, H.-X. Cui, and J. Chen, "Manipulation of dark photonic angular momentum states via magneto-optical effect for tunable slow-light performance," *Optics Express*, vol. 21, pp. 25 035–25 044, 2013.

[51] H. A. Haus and W. Huang, "Coupled-mode theory," *Proceedings of the IEEE*, vol. 79, no. 10, pp. 1505–1518, 1991.

[52] S. Fan, W. Suh, and J. D. Joannopoulos, "Temporal coupled-mode theory for the Fano resonance in optical rsonators," *J. Opt, Soc. Am. A*, vol. 20, no. 3, pp. 569–572, 2003.

[53] W. Suh, Z. Wang, and S. Fan, "Temporal coupled-mode theory and the presence of non-orthogonal modes in lossless multimode cavities," *IEEE Journal of Quantum Electronics*, vol. 40, no. 10, pp. 1511–1518, 2004.

[54] F. Giannini, M. Ruggieri, and J. Vrba, "Shunt-connected microstrip radial stubs," *IEEE Trans. Microw. Theory Tech.*, vol. 34, no. 3, pp. 363–366, 1986.

[55] C. Hoer and C. Love, "Exact inductance equations for rectangular conductors with applications to more complicated geoemetries," *J. Res. Natl. Inst. Stand. Technol.*, vol. 69C, no. 2, pp. 127–137, 1965.

[56] MATLAB, *version 9.2.0 (R2017a)*. Natick, Massachusetts: The MathWorks Inc., 2017.

[57] C.-C. Yu and K. Chang, "Transmission-line analysis of a capacitively coupled microstrip-ring resonator," *IEEE Transactions on Microwave Theory and Techniques*, vol. 45, no. 11, pp. 2018–2024, 1996.

[58] Phillips Semiconductor, *Circulators and Isolators, unique passive devices*, ser. Appl. Note AN98035, 1998.

[59] M. Cai, O. Painter, and K. J. Vahala, "Observation of critical coupling in a fiber taper to a silica-microsphere whispering-gallery mode system," *Phys. Rev. Lett.*, vol. 85, no. 1, pp. 74–77, 2000.

[60] B. D. H. Tellegen, "The gyrator, a new electrical network element," *Phillips Res. Rept.*, vol. 3, pp. 81–101, 1948.

[61] B. J. Chapman, E. I. Rosenthal, J. Kerckhoff, B. A. Moores, L. R. Vale, J. A. B. Mates, G. C. Hilton, K. Lalumiére, A. Blais, , and K. W. Lehnert, "Widely tunable on-chip microwave circulator for superconducting quantum circuits," *Phys. Rev. X*, vol. 7, p. 041043, 2017.

[62] N. Reiskarimian and H. Krishnaswamy, "Magnetic-free non-reciprocity based on staggered commutation," *Nature Communications*, vol. 7, p. 11217, 2016.

[63] S. Butterworth, "On the theory of filter amplifiers," *Experimental Wireless and Wireless Engineer*, vol. 7, pp. 536–541, 1930.